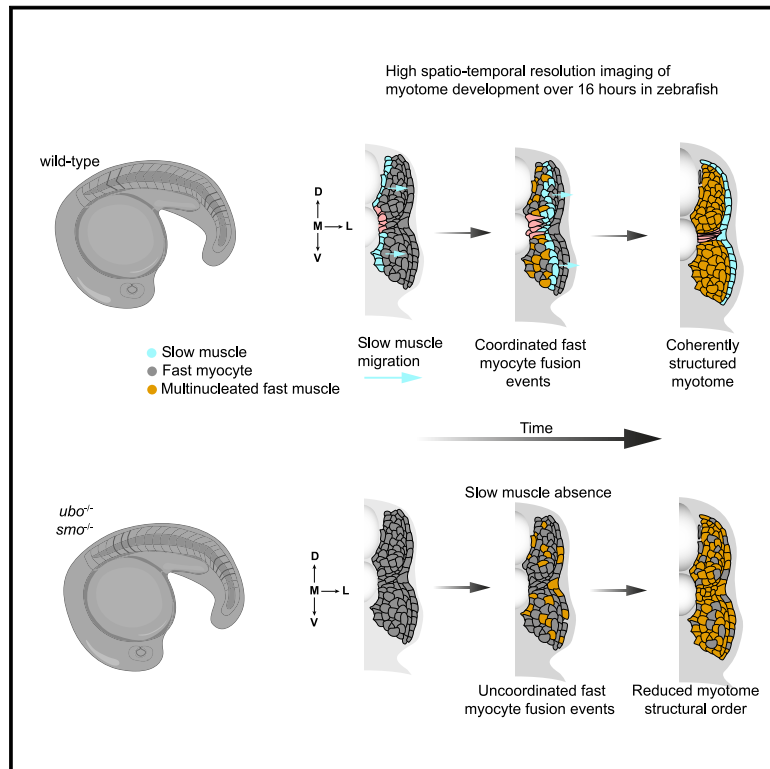


Developmental Cell

Slow muscles guide fast myocyte fusion to ensure robust myotome formation despite the high spatiotemporal stochasticity of fusion events

Graphical abstract



Authors

Mario A. Mendieta-Serrano,
Sunandan Dhar, Boon Heng Ng, ...,
Adrian Röllin, Sudipto Roy,
Timothy E. Saunders

Correspondence

sudipto@imcb.a-star.edu.sg (S.R.),
timothy.saunders@warwick.ac.uk (T.E.S.)

In brief

Mendieta-Serrano et al. report a detailed *in toto* spatiotemporal census of fast myocyte fusion during skeletal muscle development in zebrafish. Although individual fusion events are highly stochastic, slow muscle migration generates a coordinated wave of fusion at the tissue scale that ensures a robust structural positioning of multinucleated fast muscles.

Highlights

- *In toto* analysis of fast myocyte fusion in the living zebrafish embryo
- Fusion events are highly stochastic at the cellular level
- Fast myocytes present a large heterogeneity in cell shape during fusion
- Slow muscle migration organizes the spatiotemporal sequence of fast myocyte fusion



Article

Slow muscles guide fast myocyte fusion to ensure robust myotome formation despite the high spatiotemporal stochasticity of fusion events

Mario A. Mendieta-Serrano,¹ Sunandan Dhar,^{1,2} Boon Heng Ng,¹ Rachna Narayanan,^{1,2} Jorge J.Y. Lee,¹ Hui Ting Ong,¹ Pearlyn Jia Ying Toh,¹ Adrian Röllin,³ Sudipto Roy,^{4,5,6,*} and Timothy E. Saunders^{1,2,4,5,7,*}

¹Mechanobiology Institute, National University of Singapore, Singapore 117411, Singapore

²Warwick Medical School, University of Warwick, Coventry CV4 7AL, UK

³Department of Statistics and Data Science, National University of Singapore, Singapore 117546, Singapore

⁴Institute of Molecular and Cell Biology, Agency for Science, Technology and Research, Proteos, Singapore 138673, Singapore

⁵Department of Biological Sciences, National University of Singapore, Singapore 117558, Singapore

⁶Department of Paediatrics, National University of Singapore, Singapore 119228, Singapore

⁷Lead contact

*Correspondence: sudipto@imcb.a-star.edu.sg (S.R.), timothy.saunders@warwick.ac.uk (T.E.S.)

<https://doi.org/10.1016/j.devcel.2022.08.002>

SUMMARY

Skeletal myogenesis is dynamic, and it involves cell-shape changes together with cell fusion and rearrangements. However, the final muscle arrangement is highly organized with striated fibers. By combining live imaging with quantitative analyses, we dissected fast-twitch myocyte fusion within the zebrafish myotome *in toto*. We found a strong mediolateral bias in fusion timing; however, at a cellular scale, there was heterogeneity in cell shape and the relationship between initial position of fast myocytes and resulting fusion partners. We show that the expression of the fusogen *myomaker* is permissive, but not instructive, in determining the spatiotemporal fusion pattern. Rather, we observed a close coordination between slow muscle rearrangements and fast myocyte fusion. In mutants that lack slow fibers, the spatiotemporal fusion pattern is substantially noisier. We propose a model in which slow muscles *guide* fast myocytes by funneling them close together, enhancing fusion probability. Thus, despite fusion being highly stochastic, a robust myotome structure emerges at the tissue scale.

INTRODUCTION

During development, organs take on specific shapes and sizes (Coen et al., 2017; Eder et al., 2017; Saunders and Ingham, 2019). Formation of complex organ structures involves processes across scales, from subcellular interactions to tissue-scale biophysical forces, and on timescales from sub-second to hours (Lecuit et al., 2011; Narayanan et al., 2021). Cells within developing tissues often change morphology and location. These processes occur in a reproducible manner to ensure proper embryogenesis. It remains a major challenge to understand how gene expression, cell behavior, and cell signaling are all integrated to ensure robust organ formation. However, this is an important avenue of investigation, as failure of organs to form correctly results in a plethora of congenital human diseases (Bruneau, 2020; Chal and Pourquié, 2017).

Here, we focus on skeletal muscle formation. Trunk skeletal muscle derives from myotome segments, generated from the somitic mesoderm (Figure 1A; Keenan and Currie, 2019). There are two main embryonic skeletal muscle lineages: slow-twitch and fast-twitch (henceforth slow and fast) fibers, respectively (Figure 1B; Devoto et al., 1996; Schiaffino and Reggiani, 2011). In

zebrafish embryos, slow fibers are the first muscle-type to differentiate: they are specified in the medial region of the somites, juxtaposed to the notochord, and remain mono-nucleated on maturation (Devoto et al., 1996; Roy et al., 2001). A subpopulation of slow fibers migrate laterally through the somite to form a superficial layer (Cortés et al., 2003; Daggett et al., 2007; Devoto et al., 1996). Fast myocytes are initially located within the myotome bulk and fuse to become multinucleated fibers, after slow muscle differentiation is underway (Roy et al., 2001). They also undergo coordinated changes in position along both anterior-posterior (AP) and medio-lateral (ML) axes, exchanging position with the slow fibers (Henry and Amacher, 2004). Specification of these distinct lineages depends on interactions between morphogen inputs: sonic hedgehog (Shh) in the ML axis; FGF along the AP axis; and BMP in the dorsal-ventral (DV) axis (Nguyen-Chi et al., 2012; Wolff et al., 2003; Yin et al., 2018). We previously showed that timing of Shh readout is controlled non-cell autonomously by FGF, through its role in regulating slow fiber migration (Yin et al., 2018). This demonstrates a tight interconnectivity between cell movement and signaling inputs during myotome development.

Cells undergo substantial changes in shape during myotome morphogenesis. Slow fibers elongate first, with fast myocyte



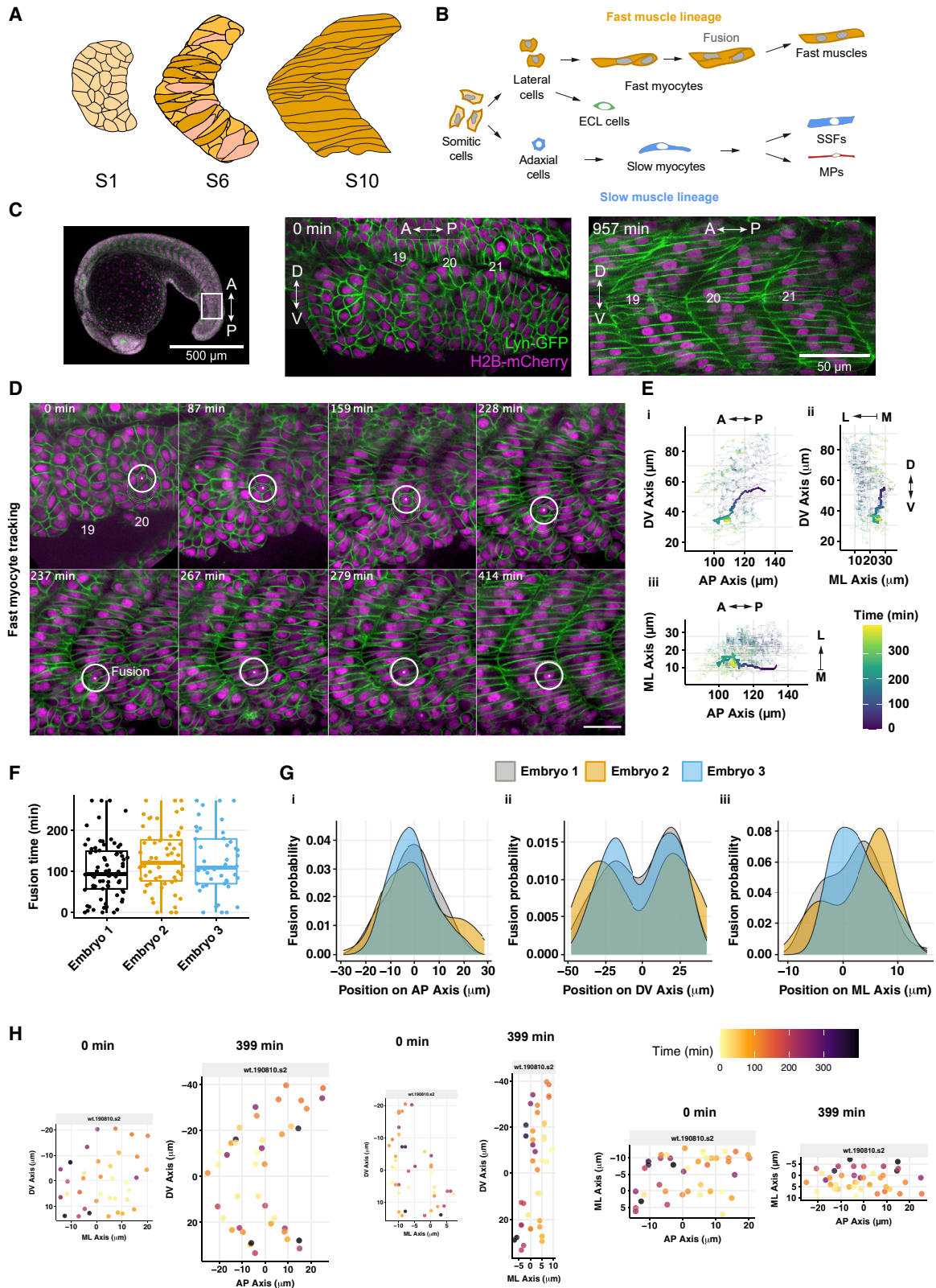


Figure 1. *In toto* quantification of cell migration and fusion events during myotome formation

(A) Schematic of zebrafish myotome development in the AP-DV plane, from immediately after somite segmentation from the PSM to formation of the initial myotome segment. Color coding highlights cell elongation.

(legend continued on next page)

elongation requiring Shh and coordination with slow fiber migration (Henry and Amacher, 2004). Basement membrane and extracellular matrix (ECM) interactions also facilitate elongation (Snow et al., 2008a, 2008b). Fast myocyte elongation occurs rapidly after “boundary capture,” when the elongating cell makes contact with segment boundaries along the AP axis (Henry and Amacher, 2004; Henry et al., 2005). Cell elongation is spatially and temporally reproducible: it is highly polarized along the AP axis, and the timing of elongation occurs in distinct patterns along the ML and DV axes (Henry and Amacher, 2004; Yin et al., 2018).

At a similar time to cell rearrangement and elongation, fast myocytes also undergo fusion. The transmembrane protein Myomaker (Mymk) (Millay et al., 2013; Zhang and Roy, 2017) and the micropeptide Myomixer (Mymx; aka Myomerger and Minion) (Bi et al., 2017; Quinn et al., 2017; Zhang et al., 2017; Shi et al., 2017) are fusogens, necessary for myocyte fusion in all vertebrates examined. However, our understanding of the regulation of these key fusogens is still incomplete. For instance, the temporal and spatial distribution of *mymk* and *mymx* expression during myogenesis in zebrafish has only been qualitatively detailed (Landemaine et al., 2014; Shi et al., 2017). There are other important components in cell fusion, including Jam2a, Jam3b (previously Jamb and Jamc, respectively), and Kirrel3l, which are thought to mediate adhesion between fusing myocytes (Powell and Wright, 2011; Srinivas et al., 2007). It has been postulated that fusion, just as with elongation, is highly coordinated in space and time (Snow et al., 2008b); for example, with fusion occurring along the AP axis (Hromowyk et al., 2020). However, this model has not been tested at a tissue scale, and there remain major unanswered questions, such as: (1) when and where do fusion events occur across the entire developing myotome? (2) How is the expression of the fusogens temporally and spatially coordinated? And (3) what role do slow fibers play, if any, in coordinating fast myocyte fusion?

Analysis of individual fusing cells suggests that fusion is biased toward elongated cells that have already connected with the segment boundary, with fusion initiating along their AP-edges (Hromowyk et al., 2020; Snow et al., 2008a). Myocyte elongation is not dependent on fusion, but the lack of fusion results in weakened adult muscle (Hromowyk et al., 2020). There is also known to be a correlation between slow muscle migration and fast muscle differentiation (Cortés et al., 2003; Henry and Amacher, 2004; Hromowyk et al., 2020; Roy et al., 2001), but the requirement of slow fibers in fast myocyte fusion has not

been directly tested. Overall, extensive work has detailed the cell-scale processes involved in forming the myotome, but how this tissue forms in a coherent manner as cells fuse and elongate remains unknown.

Here, we provide *in toto* maps of cell fusion in a living vertebrate embryo by tracking individual cells within myotome segments over 16 h. These maps allowed us to explore regions of fusion competence in unprecedented detail. We quantitatively analyzed cell-shape changes to explore links between cell shape and fusion competence. We tracked both slow and fast muscle populations to determine the relationship between the two cell types in regulating when and where fusion occurs. Strikingly, we found large heterogeneity in cell shape at fusion and also the location of the fusion site in the cell. Further, our findings suggests that at a single-cell level, fusion partners cannot be predicted based on their position after somite segmentation. Moreover, we found that *mymk* expression alone is insufficient to explain the observed spatiotemporal pattern of fusion. Instead, *mymk* defines a permissive environment in which fusion can occur. At a tissue scale, we found that the slow muscles appear to act as “guides” to the fast myocytes, ensuring they fuse in a coherent manner. Together, our work reveals how myocyte fusion, despite being highly heterogeneous at the cellular level, is coordinated in space and time by tissue-scale processes to generate a highly ordered array of multinucleated muscle fibers.

RESULTS

Generating *in toto* maps of cell fusion during myotomal myogenesis

We developed a pipeline for *in toto* analysis of the developing zebrafish myotome, which included high-resolution live imaging, nuclei tracking, data labeling, cell segmentation, and data display from somite delineation (segmentation) out of the presomitic mesoderm (PSM) through to the completion of the initial stage of myotome formation (Figures 1C and 1D; STAR Methods). Using these approaches, we were able to reliably follow somite segments 19–21 (Figures 1C and 1D; Video S1, right).

We tracked muscle cell populations in 3D, thereby creating atlases of cell position (Figures 1D and 1E; Video S2; STAR Methods). We identified slow and fast muscle cell types from their morphology and position at the end of the movies (Figures 1D and S1B–S1G; STAR Methods; Yin et al., 2018).

(B) Schematic of muscle fiber differentiation. Slow fibers remain mono-nucleated and have two subpopulations: muscle pioneers (MPs, red) and superficial slow fibers (SSFs, blue). The lateral cells differentiate mainly into the future fast fibers (orange), which become multinucleated during development, and a smaller subset that forms the external cell layer (ECL).

(C) Left: view of a 19-somite stage embryo. (Middle) Somites 19–21, just after the segmentation of somite 21 from the PSM (defined as $t = 0$). Right: somites 19–21 16 h later.

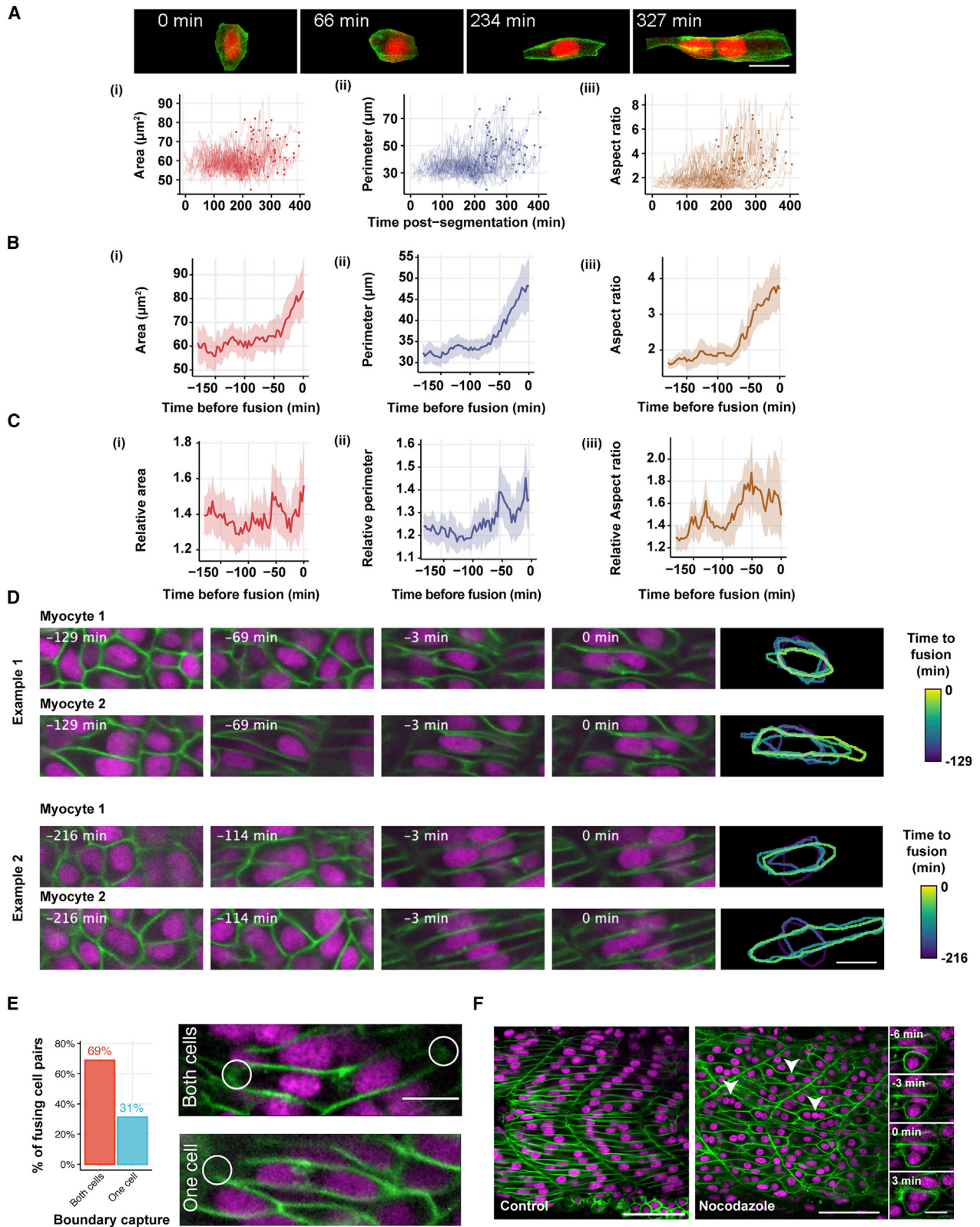
(D) Example of fast myocyte tracking. The position in the ML axis is altered to maintain the center of the nucleus in the plane shown. Scale bar, 50 μm .

(E) Tracks of fast myocytes in a complete myotome segment (orthogonal views), with the myocyte from (D) highlighted with thicker lines. Color coding represents the time from segmentation. Positions defined by the spatial coordinates from the (movement corrected) movie.

(F) Timing of fusion events. Time $t = 0$ corresponds to the first fusion event for each segment. Box represents 95% confidence interval (CI), with the bar indicating the median.

(G) Spatial distribution of fusion events in (Gi) AP, (Gii) DV, and (Giii) ML axis. Position 0 μm in each axis corresponds to the segment center. (F and G) Data from 9 segments from 3 embryos.

(H) Position of cells immediately after segmentation from the PSM ($t = 0$ min) and 400 min later for a representative segment. Color coding represents the time of individual fusion events. Positions defined as in (G).



(legend on next page)

We generated maps of cell movement from 9 complete segments from 3 embryos (3 segments per embryo), representing a total of 474 cells tracks (356 fast myocytes and 118 slow myocytes). Cell division was infrequent (52 divisions in 8 segments, over 12 h of imaging), consistent with previous findings (Bischoff and Holtzer, 1969; Gurevich et al., 2016; Tiili et al., 2019). We identified when and where each fusion event occurred for every fast myocyte tracked (Figures 1F, 1G, and S2B; Video S3).

Within each segment, the initial wave of fast myocyte fusion occurred across a 5 h window, starting about 3 h after segmentation from the PSM (Figures 1F and S2A). The large spread in the observed timing of fusion events suggests that there is potentially substantial heterogeneity in when fusion occurs (Figure 1F). Fusion events occur throughout nearly all of the developing myotome (Figures 1G and S2B). Along the AP axis, fusion occurs, on average, toward the segment center, although with a broad distribution (Figure 1Gi). Along the DV axis, fusion events display a bimodal distribution. Decrease in fusion at the DV midline is consistent with the presence there of the muscle pioneers (MPs)—a medial subpopulation of slow muscles that do not migrate (Figure 1Gii; Yin et al., 2018). In the ML axis, we see a broad spread in probability distribution and substantial embryo-to-embryo variability (Figure 1Giii). Looking at a representative somite, we compared the position of fast fibers immediately after segmentation and 400 min later (Figure 1H). Our observations suggest that the spatial location and timing of fusion at a single-cell level is not tightly determined in all axes.

We find global patterns in where fusion occurs (e.g., in DV axis), but there do not exist clear signatures of tightly correlated fusion at a cell scale. This leads to the question, if myocyte fusion is not tightly constrained in space and time, how does the myotome robustly form? Motivated by this, we next explored how cell morphology varied during muscle morphogenesis.

Cell morphospace is highly heterogeneous prior to fusion

It has been postulated that fusion occurs during or after significant cellular elongation (Snow et al., 2008a). Here, we asked whether there are cell-scale shape predictors for when and/or where fusion occurs.

Automatic segmentation is challenging, and not very accurate due to highly dynamic changes in cell morphology (Figure 2A top). Hence, we developed a custom software to provide estimates of cell boundaries, which were curated by human intervention using a graphical user interface (GUI) (STAR Methods; Figures S3A–S3C; Video S4 top). We segmented 60 cells from 4 developing myotomes. Although we did not segment every cell

within each myotome segment, we ensured that a broad range of positions were sampled.

Looking at cell shape as a function of time post segmentation, we observed large variability between cells during fusion (Figure 2A). Timing of fusion was uncorrelated with cell morphological properties (Figures 2Ai–2Aiii). We also found that the cell area, perimeter, and aspect ratio took on a wide range of values (points in Figures 2Ai–2Aii). We conclude that cell morphospace prior to fusion is highly heterogeneous and shows no correlation with the time from somite segmentation, suggesting that there is no “timer” operating to regulate fusion.

Given the coordinated action of cell elongation, we asked whether there was a relationship between cell elongation and cell fusion timing? We calculated the difference in the timing of elongation initiation, $t_{elongation}$ (defined as >20% change in aspect ratio from the averaged aspect ratio in first hour after segmentation), and the timing of fusion, t_{fusion} : $\Delta t = t_{fusion} - t_{elongation}$. We found $\Delta t = 57 \pm 32$ min; this large SD indicates that there is no clear relationship between the timing of elongation and fusion for individual cells.

We next considered whether there were hallmarks within the cell morphospace as a function of time prior to fusion. We observed that there was a sharp change in cell morphology around 60–70 min preceding fusion (Figure 2B). Cells elongated and increased both perimeter and area during this time, although with a larger relative change in the perimeter. The cell aspect ratio sharply increased around 70 min prior to fusion (Figure 2Biii). There are clear hallmarks in cell morphospace prior to fusion, but these are only weakly coordinated at tissue timescales (Figure 2A). Thus, it is unclear how a robust myotome shape emerges despite this variability.

Fusing fast myocyte pairs display large cell-to-cell morphological variability

We next asked whether cell shape was tightly correlated between fusing pairs of cells. Fusing pairs may be more intimately correlated morphologically with each other than neighboring cells.

In the case of cell area, the larger of the two fusing cells remained about 1.4 times larger up to fusion (Figure 2Ci), consistent with previous work (Snow et al., 2008a). However, the perimeter difference changed more significantly (Figure 2Cii, $p < 10^{-3}$ comparing $t = -150$ min and $t = 0$ min). Interestingly, around 90 min prior to fusion, one of the fusing cells appeared to elongate compared with its fusion partner (Figure 2Ciii; Figure S4A). Across all our segmented fusing cell pairs, ~40% had similar aspect ratio at fusion, whereas ~60% had comparatively large

Figure 2. Cell shape prior to fusion is highly heterogeneous

- (A) Top: example of images of cell shape from segmentation to fusion. Bottom: morphospace of fusing cells, defined with respect to the time from somite segmentation ($t = 0$ min). Individual dots represent the onset of fusion. Aspect ratio (Aiii) defined as the ratio of long to short axes of the best fitting ellipse to the cell cross-sectional shape. Scale bar, 10 μ m.
- (B) Morphospace of fusing cells, defined with respect to their time before fusion ($t = 0$ represents the time when each cell fused). Shaded regions indicate 95% CI.
- (C) Relative morphospace of fusing cells, where the larger value of the two cells is in the numerator at each time point (hence, relative value is always greater than 1). Shaded regions indicate 95% CI (STAR Methods). Time defined as in (B). (A–C) 60 cells, from 4 segments from 2 embryos.
- (D) Example of fusing cell pairs, highlighting the cell perimeter, with color representing time. The rounder cell is positioned on top. Time defined as in (B). Scale bar, 10 μ m.
- (E) Boundary capture analysis at fusion. 45 fusion events, from 3 myotome segments from 1 embryo. Scale bar, 10 μ m.
- (F) Image of nocodazole-treated embryo (right, control on left) injected with *lyn-gfp* and *h2b-mcherry* mRNA. Left: scale bars, 50 μ m. Right shows a close-up view of selected fused cells. Scale bars, 10 μ m. Fusion events highlighted by white arrowheads. Time defined as in (B).

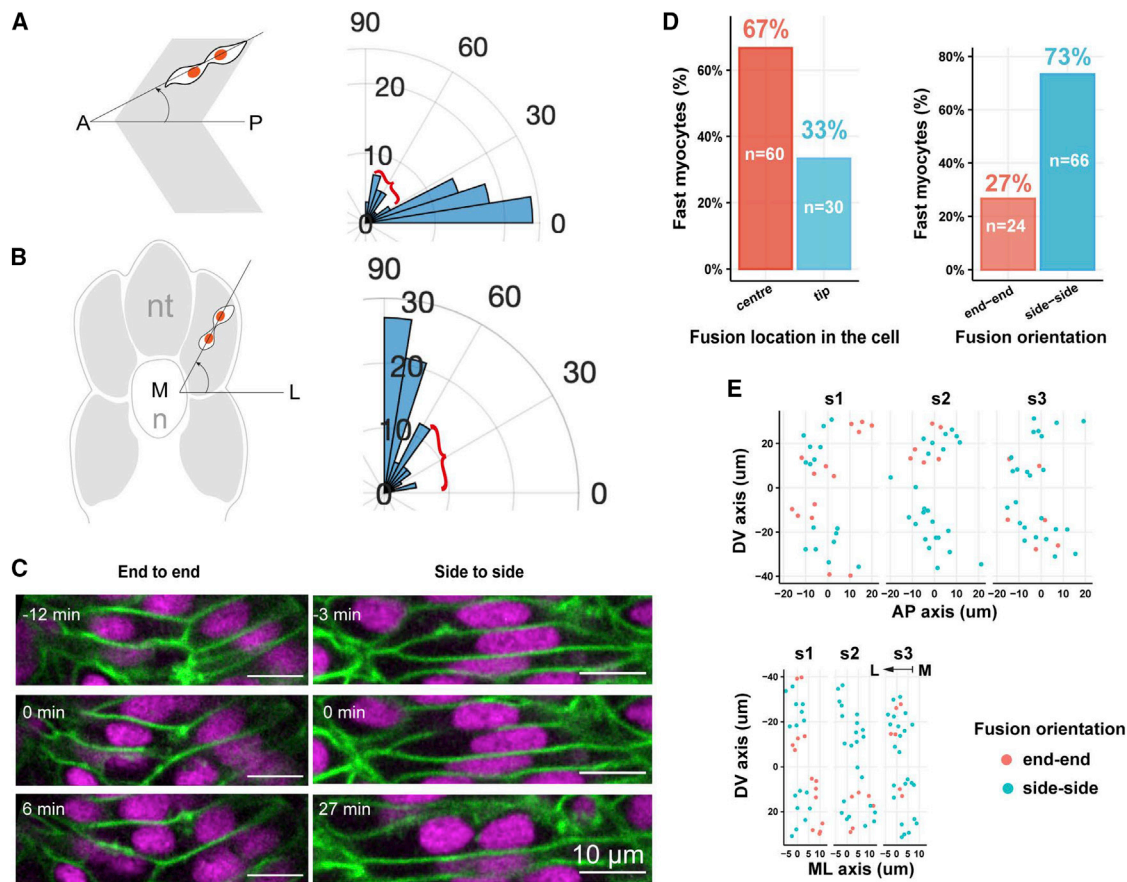


Figure 3. Cell fusion events are biased along, but not restricted to, the AP axis and do not show a local bias in position

(A) Angle of fusion events relative to tissue AP axis. Left: cartoon of angle definition, with the data distribution shown as a rose plot and the total number of events represented by increasing radius. Red bracket highlights the fraction of cells with fusion angle $>30^\circ$.

(B) As (A), but for the angle of fusion events relative to tissue ML axis. Red bracket highlights the fraction of cells with fusion angle away from ML axis by more than 30° . (A and B) 84 fusion events from 2 embryos.

(C) Example of fusion events along different axes. Left: two fast myocytes fusing end-to-end. Right: two fast myocytes fusing side-by-side. Time $t = 0$ represents fusion time.

(D) Left: location of fusion initiation within each fusing cell. Right: orientation of fusing pairs relative to each other.

(E) Distribution of end-to-end and side-to-side fusion events. Position $0 \mu\text{m}$ in each axis corresponds to the segment center, determined by the average cell position. (D and E) 90 cells, 3 myotome segments from 1 embryo.

differences in cell elongation (Figure S4B). Therefore, although the total cell size does not significantly vary, the shape of the fusing pairs is surprisingly heterogeneous (Figure 2D). These findings clarify that cell-shape changes are not harmonized between fusing pairs, and there is substantial variability within the morphospace. Thus, elongation is, by itself, not a reliable predictor of fusion capability, and furthermore, elongation is not a prerequisite for fusion.

It has been proposed that boundary capture is necessary prior to fusion (Hromowyk et al., 2020; Snow et al., 2008a). In line with this, we found that typically at least one of the fusing pair has contacted the myotome boundary (Figure 2E). However, from our *in toto* cell maps, we observed that in nearly a third of cases, only one cell was in contact with the boundary at fusion, implying that it is not necessary for both cells to have initiated boundary contact prior to fusion (Figures 2E, S4C, and S4D).

To further probe the role of elongation in fusion, we treated embryos with nocodazole (STAR Methods) to inhibit microtubule

polymerization and, consequently, prevent elongation (Saitoh et al., 1988; Zaal et al., 2011). Despite the lack of elongation, fusion remained largely unaffected (Figures 2F and S4E). We also noticed multinucleated cells that were located in the center of the myotome with no contact with myotome boundaries. Thus, neither elongation nor interaction with segment boundaries appear to be necessary conditions for fusion.

Cell fusion can initiate along any cell axis

Work with cultured cells and limited *in vivo* analysis (Hromowyk et al., 2020) suggests that cell fusion typically occurs toward the elongated region. Therefore, an alternative hypothesis for how the myotome structure emerges is that the orientation of cell fusion events is tightly regulated. To test this, we quantified the relative orientation of fusion events. Fusion was predominantly orientated along the AP axis and perpendicular to the DV and ML axes (Figures 3A and 3B). This polarized orientation of fusion may function to ensure that the fused myotubes span

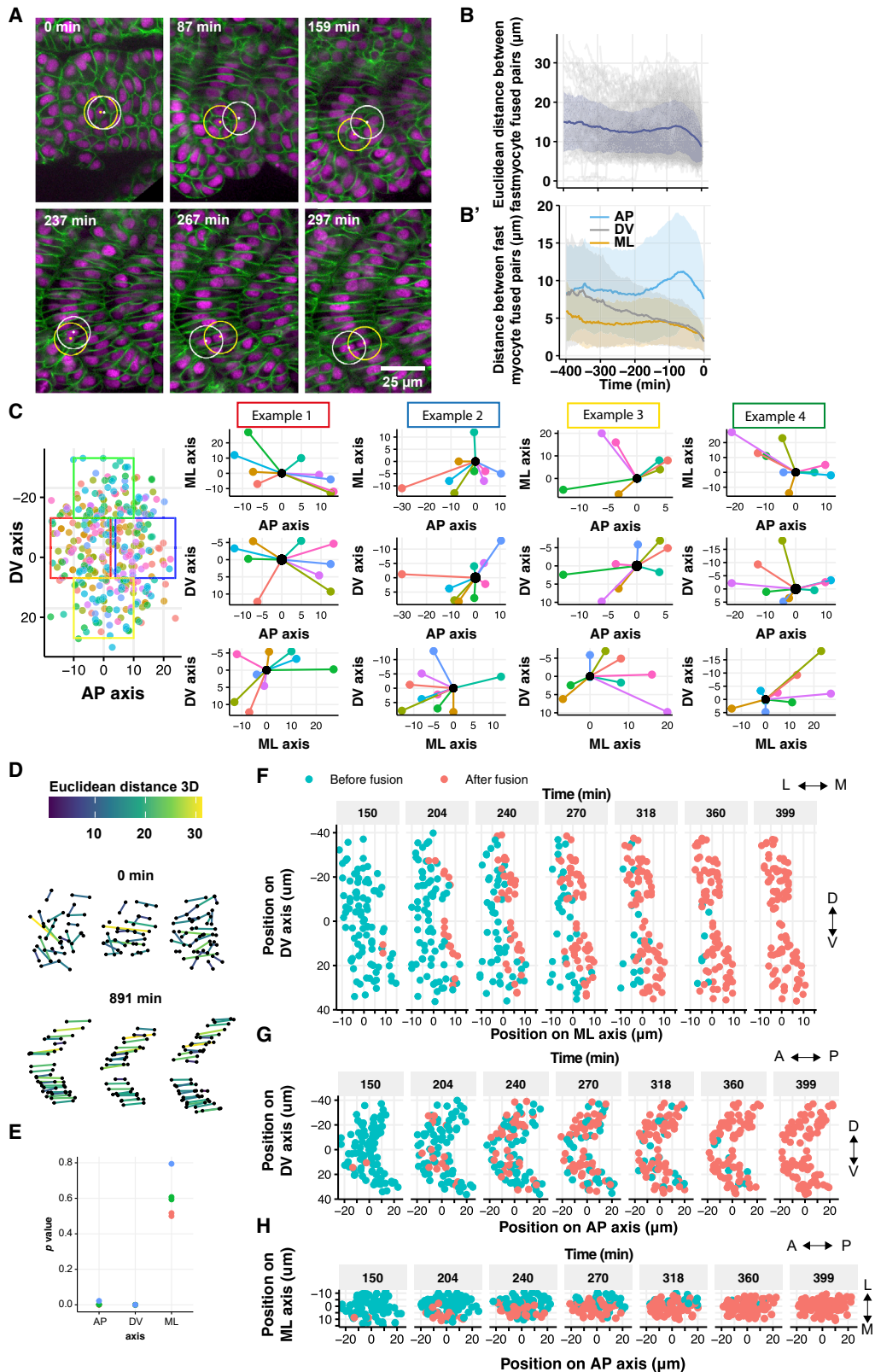


Figure 4. Fusion events cannot be predicted by initial cell position and occur in a ML wave

(A) Example of fast myocyte fusion pair tracking. ML plane chosen such that the yellow highlighted cell is kept in the observed plane. The white highlighted cell is in a different ML plane in some images (hence overlap). Time $t = 0$ represents segmentation from the PSM.

(legend continued on next page)

the AP extent of the myotome segment quickly. However, there were a notable number of fusion events (10%–20%) along different axes (brackets in Figures 3A and 3B). For example, we see “side-to-side” fusion events, where two cells fuse along the DV axis (Figure 3C; Video S4). This contrasts with myocyte elongation, which strictly occurs along the AP axis, providing additional evidence that cell elongation is not tightly linked to their fusogenic potential.

We next asked whether the location of fusion for each cell pair showed a spatial bias. We quantified the position of fusion initiation for each cell with regards to location on the cell surface, e.g., at the elongated tips or along the flatter sides (Figure 3D; STAR Methods). The point of initiation does not seem biased to specific regions of the cell; fusion events initiated in regions of both high and low membrane curvatures (Figure 3C), with multiple fusion events observed occurring at the tips and side of cells (Figure 3D). Of course, there may be global patterns in terms of where fusion initiates between fusing cells (Figure 3E). As with the timing, we see large variability in the nature of fusion events across the somites. Therefore, the particular nature of fusion events—either orientation or how cells fuse with their neighbor—does not appear to be spatially coordinated.

As a corollary, when fusion occurred in a region of low curvature, we were able to quantify the membrane retraction rate (Figure S4F; STAR Methods). This process is relatively slow (minutes) when compared with ablation of typical epithelial tissues (ms to seconds) (Toyama et al., 2008). This suggests that fast myocytes are not under high tension at the time of fusion, arguing against local cell membrane forces in determining fusion initiation sites.

We see that fast myocyte fusion is not restricted to any particular axis or cell shape, either at subcellular or cellular scales, although there is a bias toward AP-orientated fusion events. The morphospace of fusion *in vivo* is substantially more diverse than previously believed.

Cell fusion partners cannot be predicted based on the initial cell position

In *Drosophila*, “founder cells” coordinate fusion (Beckett and Baylies, 2007). Motivated by this, we asked whether there is a history dependence in the spatial or temporal fusion pattern. We also used this opportunity to test for evidence of “founder-like” behavior. The key question here being, based on initial position of cells after segmentation from the PSM, can we predict fusion partners?

For each fusing pair, they were unlikely to be neighboring immediately after somite segmentation from the PSM

(Figures 4A, 4B, and S4G). Indeed, their nuclei were typically separated by 15 μm at their maximum mean separation (roughly two cell diameters) around 90 min prior to fusion. This is especially the case along the AP axis (Figure 4B'). Fusing pairs often only physically interacted for less than 30 min prior to fusion, due in part to their elongation along the AP axis. This suggests that locality of cells immediately after segmentation plays no instructive role in determining fusing pairs. In fact, we even observed cells that divided and subsequently fused at dissimilar positions and times, suggesting that cells with the same initial morphogenetic input can exhibit different fusion behavior (Figure S4H).

To explore this idea further, we considered a fixed position relative to the center for each of our tracked somites and identified the nearest cell in each somite. We then plotted the initial positions of fusion partners associated with that cell location (Figure 4C). We show four representative examples from different positions. There was no definitive spatial relationship between a cell's initial position in the somite and the position of its future fusing partner.

The positional cues determining fusion partner could be more complicated; i.e., there may be a conserved structure in the fusion pattern at tissue scale that is lost at single-cell events. To examine this, we performed a network analysis on all of our analyzed fusing pairs, asking if the network structure immediately after somite segmentation related to the network structure at fusion (Figure 4D; STAR Methods). This analysis revealed that there is a relationship between cell position in AP and DV axes and the likelihood of which cells will fuse ($p < 10^{-2}$), i.e., cells that start in a similar AP-DV plane are more likely to fuse together than with cells from outside that region (Figure 4E, discussed further below). However, there was no correlation in the ML axis, consistent with Figures 1G and 1H.

Hence, are there founder-like cells in the developing myotome? Such cells are characterized by their ability to guide fusion, whereas the remaining muscle precursors, the fusion-competent “feeder” cells, are more passive (Ho et al., 1983; Sink, 2006). Founder cells often undergo multiple fusion events with feeders. Although we observed some multiple fusion events in the same cell during our time window of observation (Figure S4I), these were rare and appeared random in terms of locality. In contrast, we saw multiple fusion events in our nocodazole-treated embryos (arrows, Figure 2F). We do not see evidence for the existence of cells that can be identified early during myotome development that are acting as fusion centers—either with regards to their spatial position or the frequency of fusion events.

(B) Euclidean distance in 3D between fusing pairs and (B') distance between the nucleus centroid of fusing cells along different axes. Shaded regions correspond to ± 1 SD (348 cells from 3 embryos). Time $t = 0$ represents fusion time.

(C) Left: points represent cell location immediately after segmentation for a somite. Position 0 μm in each axis corresponds to the segment center, determined by average cell position. Four regions are selected within the segment (colored boxes on left). Right: for each selected region, a cell at the same location in each of the 9 somites immediately after segmentation is identified (black point). The corresponding position of the fusing partner (other colored points) was plotted from each segment, with the position of the reference cell defined as (0,0,0). As we are comparing the local position of fusing cells, we define the selected cell to be at (0,0,0) in the (AP, DV, and ML) axes.

(D) Network connections of fusing cells immediately after somite segmentation and 15 h later. Color coding represents Euclidean distance.

(E) Statistical analysis (STAR Methods) of network interactions against the null hypothesis that connections are random in each axis direction. Colors represent 3 different embryos.

(F–H) Nuclear position of fusing cells, color coded by their fusion state in DV-ML (F), DV-AP (G), and ML-AP (H) axes. Time defined as in (A). Position 0 μm in each axis corresponds to the segment center, determined by average cell position.

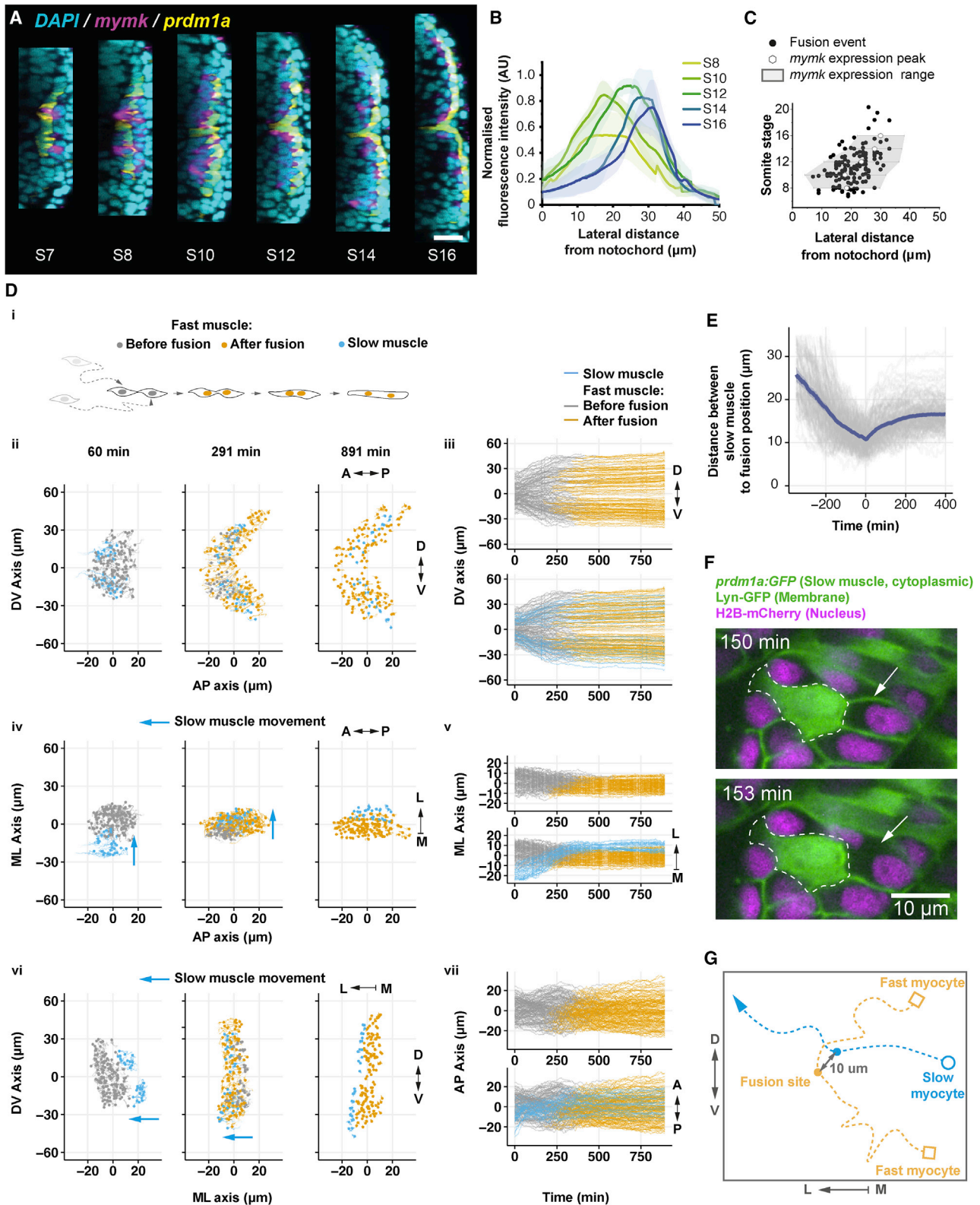


Figure 5. Slow muscle position and *mymk* expression correlate with fusion

(A) Fluorescent *in situ* hybridization (FISH) showing *mymk* expression (magenta) in a 22-somite stage embryo expressing *prdm1a::GFP*, co-stained with DAPI for labeling nuclei (cyan) and GFP (yellow, stained for anti-GFP) to mark slow fiber population. Scale bars, 20 μ m.

(legend continued on next page)

Cell fusion occurs in ML and DV waves

Although the above analysis suggests that there is large heterogeneity between fusing cells, it is possible that fusion patterns emerge at larger, tissue scales—an idea supported by the above network analysis. With regards to fast myocyte elongation, there are global spatiotemporal patterns in both the AP (Henry and Amacher, 2004) and DV axes (Yin et al., 2018). Hence, we next investigated if there are tissue-scale patterns of fusion, and, if so, whether these play a role in coordinating myotome morphogenesis.

We observed a wave of fusion from the medial to lateral domain (Figure 4F; Video S5). There is a weaker correlation along the DV axis, with fusion events occurring first more at the DV midline (Figure 4G; Video S5). We saw no clear bias in fusion timing along the AP axis (Figures 4G and 4H; Video S5). Although the ML wave is clear in all myotome segments, there is substantial heterogeneity in fusion time, even at similar ML or DV positions. This is consistent with our observations in Figure 1Giii. This result is intriguing. On one hand, our tracking and network analysis finds that predicting individual fusion events along the ML axis is not possible (Figures 4B–4E). However, there is a tissue-scale pattern in fusion along this axis (Figure 4F). This suggests that these two processes—the timing of fusion and the decision on which two specific cells will fuse—are not determined through the same mechanism. In the next sections, we will explore how fusion timing and fusion pairing are determined.

mymk expression correlates with, but does not predetermine, fusion

One mechanism for how fusion is determined may be through the fusogens, *Mymk* and *Mymx*. Do these provide sufficient spatial and temporal information in order to explain our above observations? It is known that *Mymk* is necessary and, along with *Mymx*, is sufficient to induce cell fusion, with their expression restricted to myocytes fated for fusion (Bi et al., 2017; Zhang and Roy, 2017; Shi et al., 2017; Hromowyk et al., 2020). However, previous *in vivo* analysis only provided a coarse overview of the expression profile of *mymk* during early myotome development (Landemaine et al., 2014). How intimately does fusion correlate with *mymk* expression?

Using fluorescent *in situ* hybridization (FISH, STAR Methods), we observed a ML gradient of *mymk* expression (Figures 5A, S5A, and S5B). Expression increases during the first 6 h after segmentation and then decreases in older myotome segments (Figure 5B). Expression of *mymx* also followed a similar ML gradient (Figure S5C). We mapped these results onto our identified fusion events, given the highly stereotypic timing of somite

segmentation (Figure 5C). Although fusion events do track the expression pattern of *mymk*, there is a large variability, implying that fusion is not tightly correlated with only high *mymk* expression. Although we acknowledge that *mymk* mRNA expression does not necessarily map precisely onto the levels and distribution of *Mymk* protein, quantitatively imaging endogenous *Mymk* protein dynamics *in vivo* remains challenging (see discussion). Nevertheless, our results support a model where *mymk* is necessary for defining a (rather broad) region of fusion competence, but where fusion occurs within that region is largely independent of the local *mymk* expression level.

Slow fibers appear to “guide” fast myocyte fusion

There is a tight correlation between slow muscle migratory position and fast muscle elongation (Cortés et al., 2003; Henry and Amacher, 2004; Roy et al., 2001), and previous observations have linked slow muscle position with cell fusion (Hromowyk et al., 2020). This motivates the question, does slow fiber position correlate with fusion events and subsequently are slow fibers instructive for fusion?

We compared the motion of the slow fibers and fast myocytes with the onset of cell fusion along different axes (Figure 5D; Video S6). We saw a strong correlation between slow muscle migration and fast myocyte fusion (Figure 5Dv). Strikingly, in the DV axis, slow muscles appeared like “train tracks” during fusion (Figure 5Dvii). This led us to postulate that the slow fibers act as “guides,” facilitating fusion—by defining spatial domains within which fusion-competent fast fibers can contact and fuse—rather than providing an additional cue by, for example, cell-cell signaling.

To probe this model, we analyzed the motion of fast myocytes prior to fusion with respect to the nearest slow fibers. The point of closest approach between slow fibers and fast myocytes occurs remarkably close to the onset of fusion (Figures 5E–5G). We also noticed that fusing pairs of fast myocytes always had some connection with slow fibers during fusion, although this region of overlap could be very small (Figure 5F). Consequently, we cannot discount some role for direct signaling between the slow and fast myocytes. Nevertheless, these observations imply that as slow fibers migrate through the field of fast myocytes, they provide instructional cues for where fusion can occur.

Spatiotemporal regulation of fast myocyte fusion is perturbed in the absence of slow fibers

If slow fibers are providing instructional cues for fusion timing, we hypothesized that the timing and positioning of cell fusion events in the absence of slow fibers will be less precise than in wild-type embryos, with a reduction or loss of the ML fusion

(B) FISH expression profile of *mymk* along the ML axis in different somite stages from 3 embryos, normalized by maximum *mymk* FISH intensity for each embryo and average DAPI intensity at each z stack. Position 0 μm corresponds to the notochord/myotome boundary.

(C) *mymk* expression domain (gray region, with mean \pm SD shown by hexagons and error bars, respectively) and localization of fusion events (black dots). Correlation between the FISH data and the fusion events obtained by live imaging is described in STAR Methods. Distance as in (B).

(D) (Di) Scheme showing the definition of fast myocyte fusion timing. (Dii) Position of slow and fast myocytes during fusion in DV-AP axes immediately after somite segmentation ($t = 0$ min) and at the end of imaging ($t = 891$ min). (Diii) Based on (Dii), the tracks of slow and fast myocytes from somite segmentation to fusion in the AP axis. (Div)–(Dvii) as (Dii) and (Diii) but in ML-AP axes (Div and Dv) and ML-DV axes (Dvi and Dvii). Position 0 μm in each axis corresponds to the segment center, determined by average cell position.

(E) Distance between each fast myocyte to the nearest slow muscle fiber, where $t = 0$ is determined by fusion time of each cell. 356 fast myocytes and 118 slow myocytes from 9 myotome segments from 3 embryos. Single-cell tracks shown in gray.

(F) Close-up images of fast myocyte fusion. Fusion event highlighted by arrow. Slow myocyte (expressing *prdm1a::GFP*) outlined by white dashed line.

(G) Example tracks in DV-ML plane, showing two fusing cells and path of nearest slow fiber.

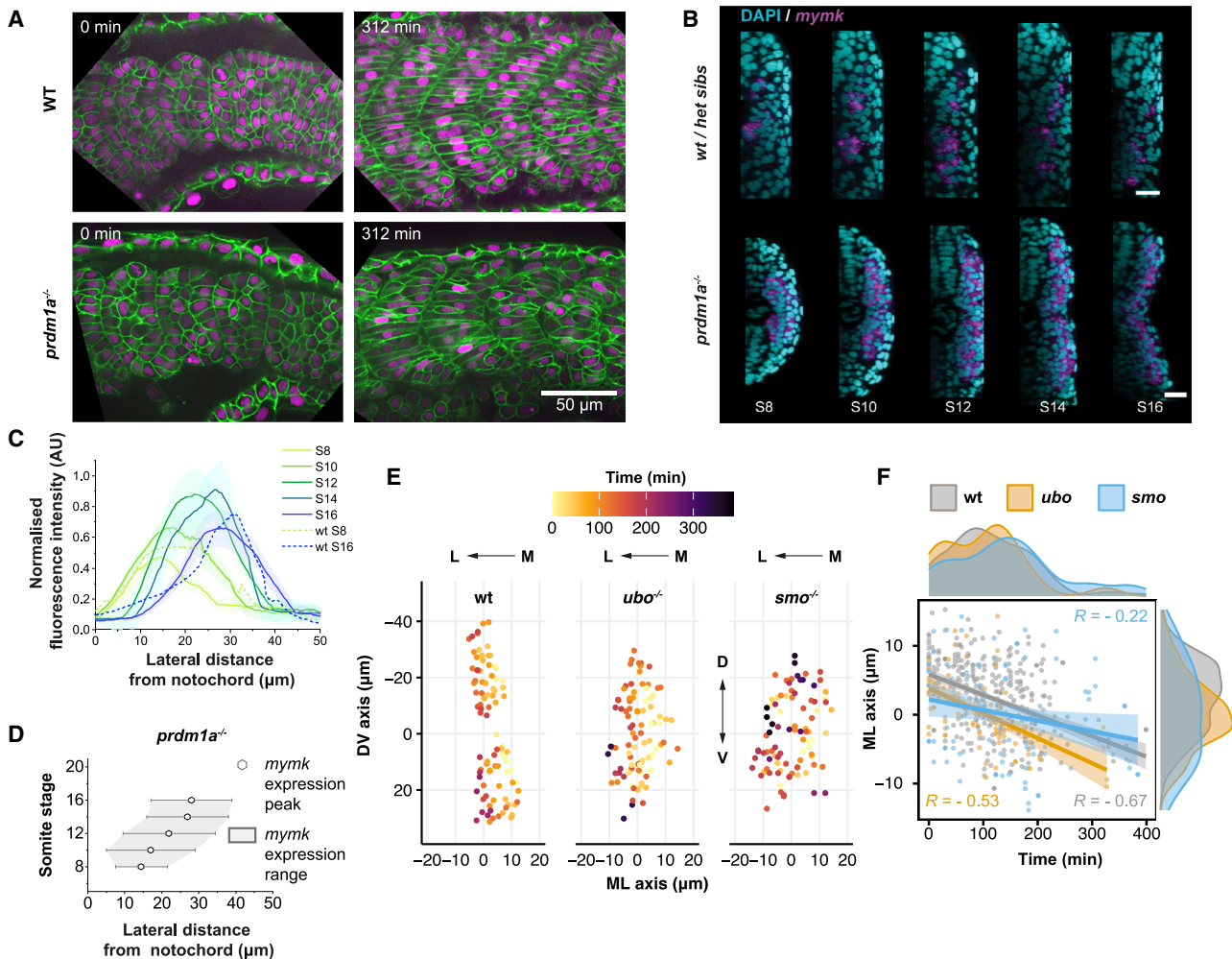


Figure 6. Loss of slow fibers results in the alteration of spatiotemporal dynamics of fast myocyte fusion

(A) *ubo* mutant at 22-somite stage expressing Lyn-GFP (cell membrane, green) and H2B-mCherry (nuclei, magenta) with sibling control. Scale bars, 50 μ m. Time $t = 0$ represents segment generation from the PSM.

(B) Localization of *mymk* expression (magenta) visualized by FISH in a *ubo* mutant embryo at 22-somite stage co-stained with DAPI (nuclei, cyan), with sibling control. Scale bars, 20 μ m.

(C) Expression profile of *mymk* along the ML axis in different somite stages of *ubo* mutant embryos. Data from three embryos, with intensity normalized as Figure 5B. Dashed lines show comparison for wild-type embryos (from Figure 5B) in S8 and S16. Position 0 μ m corresponds to the notochord/myotome boundary.

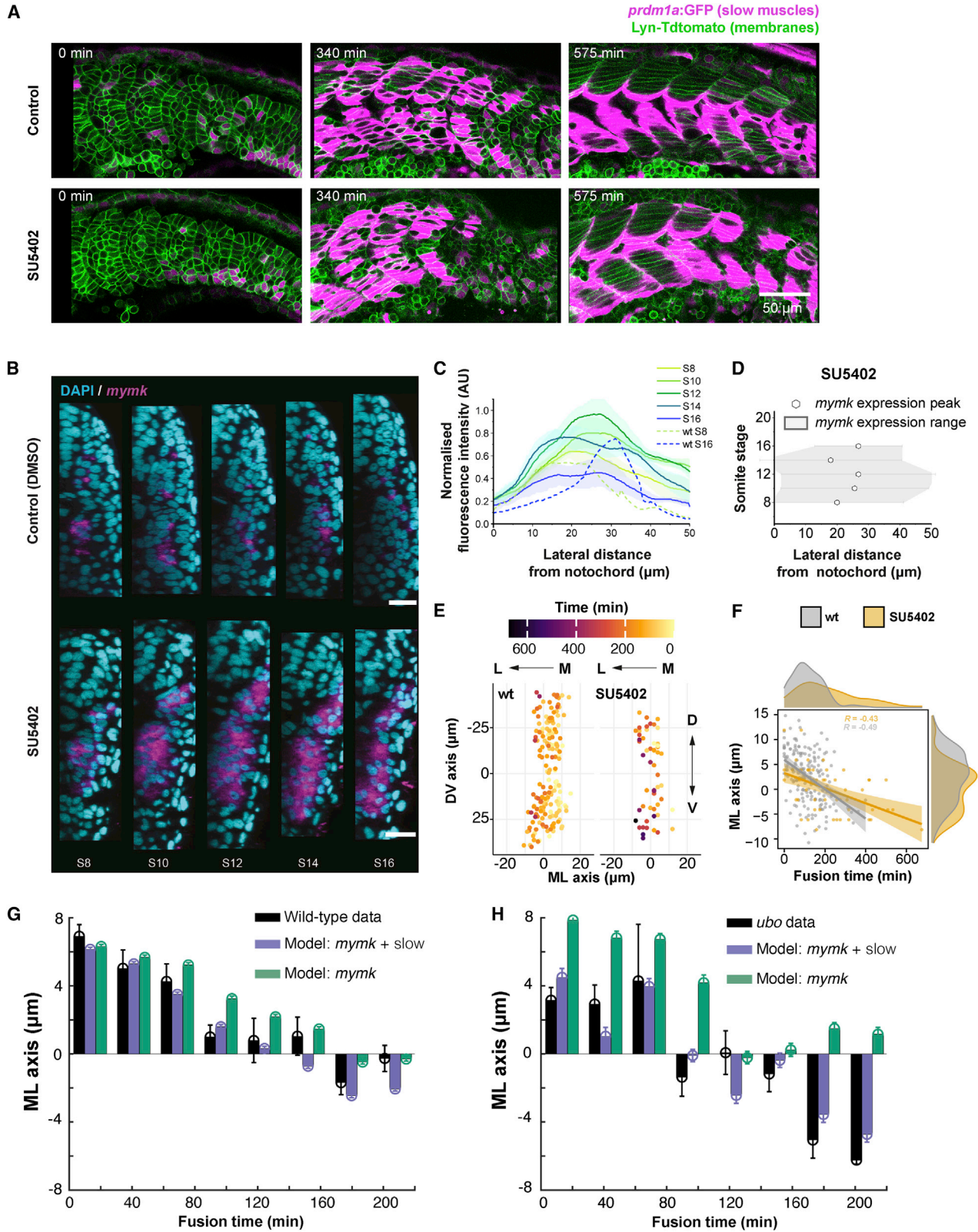
(D) *mymk* expression domain (gray region, with mean \pm SD shown by hexagons and error bars, respectively) in *ubo* mutants in the ML axis at different somite stages. Data from 3 embryos, distance as in (C).

(E) Spatial distribution of fusion events in DV-ML axes in wild-type, *ubo*, and *smo* mutant embryos. Nuclei positions at the time of fusion color coded by time normalized to the first fusion event per individual myotome. Position 0 μ m in each axis corresponds to segment center, determined by average cell position.

(F) Timing of fusion events along ML axis in wild-type, *ubo*, and *smo* embryos. Darker colored lines represent linear fit, with lighter colored regions denoting the 95% CI. Time $t = 0$ min defined by the first fusion event, and ML position 0 μ m corresponds to average cell position in ML axis for each segment. (E and F) Wild-type (179 fusion events from 9 myotomes from 3 embryos), *ubo*⁻ (45 fusion events from 3 myotomes from 1 embryo), and *smo* (46 fusion events from 3 myotomes from 1 embryo).

wave. To examine this, we first analyzed *u-boot* (*ubo*) embryos, which are deficient in the activity of the transcriptional regulator Prdm1a (Baxendale et al., 2004). Prdm1a function is restricted to the slow lineage, and *ubo* embryos fail to generate differentiated slow fibers, but fast myocyte fusion still occurs (Figure 6A; Video S7 top). Slow myocytes, the adaxial cells, which are normally fusion incompetent, instead trans-fate in *ubo* mutants and fuse to form fast muscles (Roy et al., 2001).

We checked the expression pattern of *mymk* in *ubo* embryos (Figure 6B). Consistent with previous work (Hromowyk et al., 2020), we found ectopic *mymk* expression in adaxial cells, but the graded ML distribution of *mymk* was still present and similar to wild-type (Figures 6C and 6D). Furthermore, there was a broad spread in the ML axis of *mymk* expression (gray region, Figure 6D). If the spatiotemporal distribution of *mymk* is the primary determinant for when and where fusion occurs, we would expect



(legend on next page)

ubo embryos to have similar fusion patterns to the wild-type. We tracked and examined the fusion pattern in *ubo* mutants (Figure 6E). The total number of fusion events per somite were similar compared with wild-type embryos (37 and 33 per somite in wild-type and *ubo* embryos, respectively, for 10 h post segmentation), suggesting that slow fibers are not necessary for the fusion process itself. A ML-bias in the timing of fusion events was still present, but the spatial distribution of fusion events was substantially more heterotypic, with a greater variation in fusion location along the ML axis (Figure 6F), although there was a trend of medial-to-lateral fusion. However, there was large variability in fusion events within each genotype (dots in Figure 6F). The distribution of fusion timing after segmentation from the PSM was also altered, with fusion events occurring earlier, on average, than in wild-type embryos (Figure S6D).

To further test the role of the slow muscles in regulating fast myocyte fusion, we considered a more severe perturbation to their differentiation. *Prdm1a* lies downstream of Shh signaling, and in *ubo* mutants, Shh activity remains intact (Roy et al., 2001). Hence, we next analyzed fusion in *smoothened* (*smo*) mutants where Hh signaling is abolished, thereby completely removing slow fibers, and the myotome differentiates exclusively into fast muscle (Baxendale et al., 2004; Wolff et al., 2003). The pattern of *mymk* expression was similar to *ubo* mutants (Figures S6A–S6E), albeit with more medial expression of *mymk* and a starker decrease in expression by somite stage 16, likely due to the increased fast myocyte population in the medial region. There was an average of 34 fusion events per somite for 10 h post segmentation, similar to wild-type embryos. The ML-bias of *mymk* expression was maintained, but it was more restricted, suggesting a weak role of Shh in determining the pattern of *mymk* expression, consistent with previous observations (Ganassi et al., 2018). We identified where and when fusion occurred in *smo* mutants (Figure 6E; Video S7 middle) and found that the spatiotemporal coordination of fusion became significantly noisier than even *ubo* mutants (compare spread of blue and gray points in Figure 6F).

We then examined the spatial distribution of fusion events. In wild-type embryos, there is a bias toward more medial regions ($p < 10^{-2}$, one sample t test) for fusion to occur (gray region in the right-hand probability distribution in Figure 6F). However, both *ubo* and *smo* mutants exhibited a more equal distribution along the ML axis (both $p > 0.05$, one sample t test), and the spatial

pattern was altered along the DV axis. In wild-type embryos, as described above, there is a bimodal distribution around the DV midline (Figure 1Gii). In *ubo* mutants, the bimodality was less pronounced and was completely absent in *smo* mutants (Figure 6E). Although the average timing of fusion events and the distribution of *mymk* is not strikingly different in the three genotypes, there is a clear change in the pattern of fusion events that correlates with the position and movement (or lack) of the slow muscles.

Disruption of fast muscle specification leads to fusion defects

The balance between the two slow fiber populations, the MPs and superficial slow fibers (SSFs), is controlled via FGF-mediated fast muscle rearrangements (Yin et al., 2018). Motivated by this, we predicted that perturbation of FGF signaling will alter the pattern of fast myocyte fusion by altering the relative position of slow and fast fibers.

We inhibited FGF signaling using SU5402 (which blocks FGFR, STAR Methods) in embryos expressing *prdm1a::GFP* (Figure 7A; Video S7 bottom) and imaged *mymk* expression (Figures 7B and S6E). We observed that the graded pattern of *mymk* expression along the ML axis was altered (Figures 7B–7D). In particular, *mymk* expression did not spread laterally (Figure 7D), and it was distributed over a larger area (Figures 7B and 7C). Qualitatively similar results were seen for *mymx* expression (Figure S6F).

Fusion events still displayed a ML-bias in SU5402 treated embryos, but the timing of fusion was severely disrupted, with the initial wave of fusion taking place over a longer period than in wild-type embryos (Figures 7E and 7F), as shown by the more spread probability distribution in Figure 7F (top, gray contour). This is consistent with delayed slow muscle migration in SU5402 treated embryos (Yin et al., 2018). The number of fusion events were 32 per somite for 10 h post segmentation, comparable with wild-type. We note that FGF perturbation also affects fast fibers; hence, care must be taken in interpreting these data, but in our experiments, the perturbation to cell migration was more apparent than any changes in fast myocyte behavior prior to fusion.

Model for the timing and location of cell fusion

We posited that a combination of large cell-level stochasticity between individual fusion events with global coordination (due to slow fiber migration) results in robust formation of the

Figure 7. Spatiotemporal fusion dynamics altered by disrupting myocyte specification and rearrangements

- (A) Images of the developing myotome in SU5402-treated embryos during fusion, with wild-type control. Time $t = 0$ represents segment generation from the PSM.
- (B) Localization of *mymk* expression (magenta) visualized by FISH in an embryo treated with SU5402 (and control treated with the vehicle) and visualized at 22-somite stage co-stained with DAPI (nuclei, cyan). Scale bars, 20 μm .
- (C) Expression profile of *mymk* along the ML axis in different somite stages of SU5402-treated embryos. Data from three embryos, with intensity normalized as described in STAR Methods. Dashed lines show comparison for wild-type embryos (from Figure 5B) in S8 and S16. Position 0 μm corresponds to notochord/myotome boundary.
- (D) *mymk* expression domain (gray region, with mean \pm SD shown by hexagons and error bars, respectively) from three SU5402-treated embryos in the ML axis at different somite stages. Distance as in (C).
- (E) Spatial distribution of fusion events in DV-ML axes in SU5402-treated embryo (right) compared with wild-type (left). Fusion events color coded by time normalized to the first fusion event per individual myotome.
- (F) Timing of fusion events in SU5402-treated embryos (gray) compared with wild-type (orange). The distributions show the spread of fusion timing and spatial position in ML axis (where 0 μm corresponds to the average ML position of the cells in each segment). Time $t = 0$ defined by the first fusion event. (E and F) 9 myotome segments from 3 embryos for wild-type and 3 myotome segments from 1 embryo in SU5402 treated.
- (G and H) Model predicting the timing of fusion events along the ML axis in wild-type (G) and *ubo* (H) embryos. Black: experimental data (from Figures 5 and 6). Purple: model prediction (STAR Methods) based on both *mymk* expression and slow fiber movement. Green: model prediction (STAR Methods) based on *mymk* expression alone. Error bars = SEM. Time and position defined as in (F).

myotome that can adjust to local variations during morphogenesis. To test this mechanism of fusion coordination more decisively, we developed a 1D model for fusion along the ML axis (STAR Methods). We used *mymk* expression in each condition to define the probability distribution for fusion events. This has three important consequences: (1) fusion cannot happen in the absence of *mymk*, (2) fusion does not necessarily always occur at the highest *mymk* expression, and (3) the occurrence of fusion events has an element of randomness and is not strictly determined by *mymk* expression.

Using the *mymk* expression pattern alone to define the probability of fusion only roughly mapped onto the observed fusion events in the wild-type (Figure 7G, green bars). However, if we included a multiplier reflecting the local position of slow fibers (increase in local probability of fusion if slow fibers are nearby), then the model accurately predicted the onset of fusion (Figure 7G purple bars, Figure S6G). In *ubo* mutants, there were fewer slow fibers, and migration was delayed and noisier. Accounting for this in the model (STAR Methods), we found agreement with the pattern of fusion events in *ubo* mutants (Figures 7H and S6H). In *smo* mutants, there is a total loss of slow fibers although there is ML polarity in *mymk*. Consistent with this, the model predicted that fusion events should be more uniformly distributed through the tissue, with a small ML-bias due to *mymk* expression (Figure S6I). Finally, in SU5402-treated embryos, slow muscle migration was delayed and slower (Yin et al., 2018). The model predicted the resulting fusion pattern, although *mymk* expression was substantially altered in these embryos (Figure S6J). Our model confirms that the combination of *mymk* expression defining a region of fusion competence and slow muscles providing a scaffold to locally enhance fusion probability is sufficient to explain the observed patterns of fast myocyte fusion.

DISCUSSION

By generating *in toto* maps at cellular and tissue scales, we have comprehensively dissected the spatial and temporal dynamics of fast myocyte fusion during the first 16 h of myotome segment development in the living zebrafish embryo. Although mouse (Millay et al., 2013) and chick (Sieiro-Mosti et al., 2014) systems have provided critical insights into myocyte fusion, they do not offer the temporal or spatial imaging resolution required to visualize the fusion process in real time. Our maps provide detailed insights into how cells within a complex developing organ interact to form a robust and precisely patterned differentiated structure. Previous work had suggested that given the known waves of muscle fiber elongation, cell fusion is highly coordinated at a cellular scale, thereby leading to robust myotome formation (Henry and Amacher, 2004; Hromowyk et al., 2020). Surprisingly, our investigations have revealed that this is not the case for fusion: at a cellular scale, fusion events are stochastic, and the pattern of fusion between somite segments is highly variable (Figures 2 and 3). Moreover, neither cell elongation nor boundary capture are strictly necessary for fusion as posited earlier; however, at a tissue-scale, we found coordinated waves of fusion (Figures 4 and 5). Slow muscle migration appears to be the dominant mechanism in regulating such coordination, with cell-shape changes and *mymk* expression playing only a limited role (Figures 6 and 7).

Our results led to the following model: (1) *mymk* expression reflects the intrinsic fusion competence of fast myocytes but do not determine where/when fusion occurs, (2) slow fiber rearrangements increase the probability of fusion among contacted fusion-competent fast myocytes, and (3) slow fiber migration generates a wave of coordinated fusion at a tissue scale that ensures robust syncytial fast fiber differentiation. Besides fusion competence engendered by fusogens and the “guiding” effects of slow fibers, the ECM and adhesive environment also play important roles in myotomal morphogenesis. Interactions between myoblasts and ECM are critical for cell elongation (Snow et al., 2008b), and the ECM also plays important roles in morphogen signaling (Müller and Schier, 2011) that function in the specification of the distinct muscle lineages. Furthermore, there are gradients of cell adhesion molecules, such N-Cadherin (Cdh2) in the fast muscle precursors and M-Cadherin (Cdh15) in the adaxial cells (Cortés et al., 2003). These opposing gradients have been proposed to drive slow muscle migration through the fast myocytes, although recent work has suggested a more active, cell autonomous mechanism (Ono et al., 2015). A more complete picture for how fusion is regulated will require a deeper understanding of how cell rearrangements are controlled. The quantitative maps provided here will be an important resource in developing such models.

Recently, it has been demonstrated that F-actin localization is required for the initiation of the fusion pore in an asymmetric manner between the two fusing fast myocytes and that the localization of the adhesion protein, Jam2a, at the “fusogenic synapse” guides this focal actin polymerization (Luo et al., 2022). Interestingly, significant cell-to-cell variability in the onset of fusion pore formation was noted, reflecting our observed large-scale heterogeneities in cell shape prior to fusion. Taken together, the work of Luo et al. and our study has revealed the dynamics of myocyte fusion in an intact vertebrate *in vivo*, from tissue scale to the subcellular level. Future work must be directed toward unraveling further details of the molecular interactions and biomechanical pathways that regulate this process to generate the highly structured myotome.

Limitations of the study

Although we are confident in our data, a caveat is that it is restricted to only one time period of myotome formation, and the segmentation is limited to 2D. We have also not visualized *Mymk* protein dynamics with respect to fusion. *Mymk* topology currently prevents the generation of a functional protein with epitope tags (Luo et al., 2022). Finally, we have not explored the potential roles of the cytoskeleton and ECM in fusion coordination.

STAR★METHODS

Detailed methods are provided in the online version of this paper and include the following:

- KEY RESOURCES TABLE
- RESOURCE AVAILABILITY
 - Lead contact
 - Materials availability

- Data and code availability
- **EXPERIMENTAL MODEL AND SUBJECT DETAILS**
 - Zebrafish husbandry
- **METHOD DETAILS**
 - Time-lapse imaging
 - Somite alignment
 - Mutant analysis
 - Drug treatments
 - Cell tracking protocol
 - Cell segmentation
 - Fluorescent *in situ* hybridisation
- **QUANTIFICATION AND STATISTICAL ANALYSIS**
 - Figure 2
 - Figure 3
 - Figure 4
 - Figure 5
 - Figure 6
 - Figure 7
 - Stochastic model of cell fusion

SUPPLEMENTAL INFORMATION

Supplemental information can be found online at <https://doi.org/10.1016/j.devcel.2022.08.002>.

ACKNOWLEDGMENTS

This work was funded by a Singapore Ministry of Education Tier 3 grant (MOE2016-T3-1-005), an EMBO Global Investigator Award, University of Warwick startup support to T.E.S., and the Agency for Science, Technology, and Research, Singapore (A*STAR), to S.R. We acknowledge IMCB fish facility staff and MBI Microscopy, Computing, and Wet-lab support teams.

AUTHOR CONTRIBUTIONS

M.A.M.-S., S.R., and T.E.S. conceived the project. M.A.M.-S., S.D., B.H.N., R.N., P.J.Y.T., S.R., and T.E.S. planned experiments. M.A.M.-S., S.D., B.H.N., and P.J.Y.T. performed the experiments. S.D. carried out the FISH experiments with guidance from R.N. and S.R. J.J.Y.L., H.T.O., and M.A.M.-S. developed the image analysis tools. M.A.M.-S., S.D., and B.H.N. carried out cell tracking and segmentation. Data analysis was performed by M.A.M.-S. with assistance from A.R. and T.E.S. S.D., M.A.M.-S., and T.E.S. made the figures. M.A.M.-S., S.R., and T.E.S. wrote the manuscript with R.N. providing critical input. All authors reviewed the final manuscript.

DECLARATION OF INTERESTS

The authors declare no competing interests.

Received: September 8, 2021

Revised: June 7, 2022

Accepted: August 5, 2022

Published: August 25, 2022

REFERENCES

Baxendale, S., Davison, C., Muxworthy, C., Wolff, C., Ingham, P.W., and Roy, S. (2004). The B-cell maturation factor Blimp-1 specifies vertebrate slow-twitch muscle fiber identity in response to Hedgehog signaling. *Nat. Genet.* *36*, 88–93. <https://doi.org/10.1038/ng1280>.

Beckett, K., and Bayliss, M.K. (2007). 3D analysis of founder cell and fusion competent myoblast arrangements outlines a new model of myoblast fusion. *Dev. Biol.* *309*, 113–125. <https://doi.org/10.1016/j.ydbio.2007.06.024>.

Bi, P., Ramirez-Martinez, A., Li, H., Cannavino, J., McAnally, J.R., Shelton, J.M., Sánchez-Ortiz, E., Bassel-Duby, R., and Olson, E.N. (2017). Control of

muscle formation by the fusogenic micropeptide myomixer. *Science* *356*, 323–327. <https://doi.org/10.1126/science.aam9361>.

Bischoff, R., and Holtzer, H. (1969). Mitosis and the processes of differentiation of myogenic cells *in vitro*. *J. Cell Biol.* *41*, 188–200. <https://doi.org/10.1083/jcb.41.1.188>.

Bruneau, B.G. (2020). The developing heart: from The Wizard of Oz to congenital heart disease. *Development* *147*, dev194233–dev194236. <https://doi.org/10.1242/dev.194233>.

Bunn, A., and Korpela, M. (2019). An introduction to *dplR2021*.

Chal, J., and Pourquié, O. (2017). Making muscle: skeletal myogenesis *in vivo* and *in vitro*. *Development* *144*, 2104–2122. <https://doi.org/10.1242/dev.151035>.

Chen, W., Burgess, S., and Hopkins, N. (2001). Analysis of the zebrafish smoothed mutant reveals conserved and divergent functions of hedgehog activity. *Development* *128*, 2385–2396. <https://doi.org/10.1242/dev.128.12.2385>.

Coen, E., Kennaway, R., and Whitewoods, C. (2017). On genes and form. *Development* *144*, 4203–4213. <https://doi.org/10.1242/dev.151910>.

Cortés, F., Daggett, D., Bryson-Richardson, R.J., Neyt, C., Maule, J., Gautier, P., Hollway, G.E., Keenan, D., and Currie, P.D. (2003). Cadherin-mediated differential cell adhesion controls slow muscle cell migration in the developing zebrafish myotome. *Dev. Cell* *5*, 865–876. [https://doi.org/10.1016/S1534-5807\(03\)00362-9](https://doi.org/10.1016/S1534-5807(03)00362-9).

Daggett, D.F., Domingo, C.R., Currie, P.D., and Amacher, S.L. (2007). Control of morphogenetic cell movements in the early zebrafish myotome. *Dev. Biol.* *309*, 169–179. <https://doi.org/10.1016/j.ydbio.2007.06.008>.

Devoto, S.H., Melançon, E., Eisen, J.S., and Westerfield, M. (1996). Identification of separate slow and fast muscle precursor cells *in vivo*, prior to somite formation. *Development* *122*, 3371–3380.

Eder, D., Aegerter, C., and Basler, K. (2017). Forces controlling organ growth and size. *Mech. Dev.* *144*, 53–61. <https://doi.org/10.1016/j.mod.2016.11.005>.

Elworthy, S., Hargrave, M., Knight, R., Mebus, K., and Ingham, P.W. (2008). Expression of multiple slow myosin heavy chain genes reveals a diversity of zebrafish slow twitch muscle fibres with differing requirements for Hedgehog and Prdm1 activity. *Development* *135*, 2115–2126. <https://doi.org/10.1242/dev.015719>.

Ganassi, M., Badodi, S., Ortuste Quiroga, H.P., Zammit, P.S., Hinits, Y., and Hughes, S.M. (2018). Myogenin promotes myocyte fusion to balance fibre number and size. *Nat. Commun.* *9*, 4232. <https://doi.org/10.1038/s41467-018-06583-6>.

Gurevich, D.B., Nguyen, P.D., Siegel, A.L., Ehrlich, O.V., Sonntag, C., Phan, J.M.N., Berger, S., Ratnayake, D., Hersey, L., Berger, J., et al. (2016). Asymmetric division of clonal muscle stem cells coordinates muscle regeneration *in vivo*. *Science* *353*, aad9969. <https://doi.org/10.1126/science.aad9969>.

Henry, C.A., and Amacher, S.L. (2004). Zebrafish slow muscle cell migration induces a wave of fast muscle morphogenesis. *Dev. Cell* *7*, 917–923. <https://doi.org/10.1016/j.devcel.2004.09.017>.

Henry, C.A., McNulty, I.M., Durst, W.A., Munchel, S.E., and Amacher, S.L. (2005). Interactions between muscle fibers and segment boundaries in zebrafish. *Dev. Biol.* *287*, 346–360. <https://doi.org/10.1016/j.ydbio.2005.08.049>.

Ho, R.K., Ball, E.E., and Goodman, C.S. (1983). Muscle pioneers: large mesodermal cells that erect a scaffold for developing muscles and motoneurons in grasshopper embryos. *Nature* *307*, 66–69. <https://doi.org/10.1038/301066a0>.

Hromowyk, K.J., Talbot, J.C., Martin, B.L., Janssen, P.M.L., and Amacher, S.L. (2020). Cell fusion is differentially regulated in zebrafish post-embryonic slow and fast muscle. *Dev. Biol.* *462*, 85–100. <https://doi.org/10.1016/j.ydbio.2020.03.005>.

Hunter, D.R., Handcock, M.S., Butts, C.T., Goodreau, S.M., and Morris, M. (2008). *ergm*: A Package to Fit, Simulate and Diagnose Exponential-Family Models for Networks. *J. Stat. Softw.* *24*, nihpa54860. <https://doi.org/10.18637/jss.v024.i03>.

Keenan, S.R., and Currie, P.D. (2019). The developmental phases of zebrafish myogenesis. *J. Dev. Biol.* *7*, 12–21. <https://doi.org/10.3390/jdb7020012>.

- Kimmel, C.B., Ballard, W.W., Kimmel, S.R., Ullmann, B., and Schilling, T.F. (1995). Stages of embryonic development of the zebrafish. *Dev. Dyn.* *203*, 253–310. <https://doi.org/10.1002/aja.1002030302>.
- Landemaine, A., Rescan, P.-Y., and Gabillard, J.-C. (2014). Myomaker mediates fusion of fast myocytes in zebrafish embryos. *Biochem. Biophys. Res. Commun.* *451*, 480–484. <https://doi.org/10.1016/j.bbrc.2014.07.093>.
- Lecuit, T., Lenne, P.-F., and Munro, E. (2011). Force generation, transmission, and integration during cell and tissue morphogenesis. *Annu. Rev. Cell Dev. Biol.* *27*, 157–184.
- Lucy, L.B. (1974). An iterative technique for the rectification of observed distributions. *Astron. J.* *79*, 745.
- Luo, Z., Shi, J., Pandey, P., Ruan, Z.-R., Sevdali, M., Bu, Y., Lu, Y., Du, S., and Chen, E.H. (2022). The cellular architecture and molecular determinants of the zebrafish fusogenic synapse. *Dev. Cell* *57*, 1582–1597.e6. <https://doi.org/10.1016/j.devcel.2022.05.016>.
- Meijering, E., Dzyubachyk, O., and Smal, I. (2012). Methods for cell and particle tracking. *Methods Enzymol.* *504*, 183–200. <https://doi.org/10.1016/B978-0-12-391857-4.00009-4>.
- Millay, D.P., O'Rourke, J.R., Sutherland, L.B., Bezprozvannaya, S., Shelton, J.M., Bassel-Duby, R., and Olson, E.N. (2013). Myomaker is a membrane activator of myoblast fusion and muscle formation. *Nature* *499*, 301–305. <https://doi.org/10.1038/nature12343>.
- Müller, P., and Schier, A.F. (2011). Extracellular movement of signaling molecules. *Dev. Cell* *21*, 145–158. <https://doi.org/10.1016/j.devcel.2011.06.001>.
- Narayanan, R., Mendieta-Serrano, M.A., and Saunders, T.E. (2021). The role of cellular active stresses in shaping the zebrafish body axis. *Curr. Opin. Cell Biol.* *73*, 69–77.
- Narayanan, R., and Oates, A.C. (2019). Detection of mRNA by Whole Mount in situ Hybridization and DNA Extraction for Genotyping of zebrafish Embryos. *Bio Protoc.* *9*, e3193. <https://doi.org/10.21769/BioProtoc.3193>.
- Nguyen-Chi, M.E., Bryson-Richardson, R., Sonntag, C., Hall, T.E., Gibson, A., Sztal, T., Chua, W., Schilling, T.F., and Currie, P.D. (2012). Morphogenesis and cell fate determination within the adaxial cell equivalence group of the zebrafish myotome. *PLoS Genet.* *8*, e1003014. <https://doi.org/10.1371/journal.pgen.1003014>.
- Ono, Y., Yu, W., Jackson, H.E., Parkin, C.A., and Ingham, P.W. (2015). Adaxial cell migration in the zebrafish embryo is an active cell autonomous property that requires the Prdm1a transcription factor. *Differentiation* *89*, 77–86. <https://doi.org/10.1016/j.diff.2015.03.002>.
- Parslow, A., Cardona, A., and Bryson-Richardson, R.J. (2014). Sample drift correction following 4D confocal time-lapse imaging. *J. Vis. Exp.* *12*, 51086. <https://doi.org/10.3791/51086>.
- Powell, G.T., and Wright, G.J. (2011). Jamb and Jamc are essential for vertebrate myocyte fusion. *PLoS Biol.* *9*, e1001216. <https://doi.org/10.1371/journal.pbio.1001216>.
- Quinn, M.E., Goh, Q., Kurosaka, M., Gamage, D.G., Petrazy, M.J., Prasad, V., and Millay, D.P. (2017). Myomerger induces fusion of non-fusogenic cells and is required for skeletal muscle development. *Nat. Commun.* *8*, 15665.
- Richardson, W.H. (1972). Bayesian-based iterative method of image restoration. *J. Opt. Soc. Am.* *62*, 55–59. <https://doi.org/10.1364/JOSA.62.000055>.
- Roy, S., Wolff, C., and Ingham, P.W. (2001). The u-boot mutation identifies a Hedgehog-regulated myogenic switch for fiber-type diversification in the zebrafish embryo. *Genes Dev.* *15*, 1563–1576. <https://doi.org/10.1101/gad.195801>.
- Saitoh, O., Arai, T., and Obinata, T. (1988). Distribution of microtubules and other cytoskeletal filaments during myotube elongation as revealed by fluorescence microscopy. *Cell Tissue Res.* *252*, 263–273. <https://doi.org/10.1007/BF00214368>.
- Saunders, T.E., and Ingham, P.W. (2019). Open questions: how to get developmental biology into shape? *BMC Biol.* *17*, 17. <https://doi.org/10.1186/s12915-019-0636-6>.
- Schiaffino, S., and Reggiani, C. (2011). Fiber types in mammalian skeletal muscles. *Physiol. Rev.* *91*, 1447–1531. <https://doi.org/10.1152/physrev.00031.2010>.
- Schindelin, J., Arganda-Carreras, I., Frise, E., Kaynig, V., Longair, M., Pietzsch, T., Preibisch, S., Rueden, C., Saalfeld, S., Schmid, B., et al. (2012). Fiji: an open-source platform for biological-image analysis. *Nat. Methods* *9*, 676–682. <https://doi.org/10.1038/nmeth.2019>.
- Shi, J., Bi, P., Pei, J., Li, H., Grishin, N.V., Bassel-Duby, R., Chen, E.H., and Olson, E.N. (2017). Requirement of the fusogenic micropeptide myomixer for muscle formation in zebrafish. *Proc. Natl. Acad. Sci. USA* *114*, 11950–11955. <https://doi.org/10.1073/pnas.1715229114>.
- Sieiro-Mosti, D., De La Celle, M., Pelé, M., and Marcelle, C. (2014). A dynamic analysis of muscle fusion in the chick embryo. *Development* *141*, 3605–3611. <https://doi.org/10.1242/dev.114546>.
- Sink, H. (2006). *Muscle Development in Drosophila* (Springer). <https://doi.org/10.1007/0-387-32963-3>.
- Snow, C.J., Goody, M., Kelly, M.W., Oster, E.C., Jones, R., Khalil, A., and Henry, C.A. (2008a). Time-lapse analysis and mathematical characterization elucidate novel mechanisms underlying muscle morphogenesis. *PLoS Genet.* *4*, e1000219. <https://doi.org/10.1371/journal.pgen.1000219>.
- Snow, C.J., Peterson, M.T., Khalil, A., and Henry, C.A. (2008b). Muscle development is disrupted in zebrafish embryos deficient for fibronectin. *Dev. Dyn.* *237*, 2542–2553. <https://doi.org/10.1002/dvdy.21670>.
- Srinivas, B.P., Woo, J., Leong, W.Y., and Roy, S. (2007). A conserved molecular pathway mediates myoblast fusion in insects and vertebrates. *Nat. Genet.* *39*, 781–786. <https://doi.org/10.1038/ng2055>.
- Thévenaz, P., Ruttimann, U.E., and Unser, M. (1998). A pyramid approach to subpixel registration based on intensity. *IEEE Trans. Image Process.* *7*, 27–41. <https://doi.org/10.1109/83.650848>.
- Tlili, S., Yin, J., Rupprecht, J.F., Mendieta-Serrano, M.A., Weissbart, G., Verma, N., Teng, X., Toyama, Y., Prost, J., and Saunders, T.E. (2019). Shaping the zebrafish myotome by intertissue friction and active stress. *Proc. Natl. Acad. Sci. USA* *116*, 25430–25439. <https://doi.org/10.1073/pnas.1900819116>.
- Toyama, Y., Peralta, X.G., Wells, A.R., Kiehart, D.P., and Edwards, G.S. (2008). Apoptotic force and tissue dynamics During drosophila embryogenesis. *Science* *321*, 1683–1686. <https://doi.org/10.1126/science.1157052>.
- van Eeden, F.J., Granato, M., Schach, U., Brand, M., Furutani-Seiki, M., Haffter, P., Hammerschmidt, M., Heisenberg, C.P., Jiang, Y.J., Kane, D.A., et al. (1996). Mutations affecting somite formation and patterning in the zebrafish, *Danio rerio*. *Development* *123*, 153–164.
- Wolff, C., Roy, S., and Ingham, P.W. (2003). Multiple muscle cell identities induced by distinct levels and timing of hedgehog activity in the zebrafish embryo. *Curr. Biol.* *13*, 1169–1181. [https://doi.org/10.1016/S0960-9822\(03\)00461-5](https://doi.org/10.1016/S0960-9822(03)00461-5).
- Yin, J., Lee, R., Ono, Y., Ingham, P.W., and Saunders, T.E. (2018). Spatiotemporal coordination of FGF and Shh signaling underlies the specification of myoblasts in the zebrafish embryo. *Dev. Cell* *46*, 735–750.e4. <https://doi.org/10.1016/j.devcel.2018.08.024>.
- Zaal, K.J.M., Reid, E., Mousavi, K., Zhang, T., Mehta, A., Bugnard, E., Sartorelli, V., and Ralston, E. (2011). Who needs microtubules? Myogenic reorganization of MTOC, Golgi complex and ER exit sites persists despite lack of normal microtubule tracks. *PLoS One* *6*, e29057. <https://doi.org/10.1371/journal.pone.0029057>.
- Zhang, Q., Vashisht, A.A., O'Rourke, J., Corbel, S.Y., Moran, R., Romero, A., Miraglia, L., Zhang, J., Durrant, E., Schmedt, C., et al. (2017). The microprotein Minion controls cell fusion and muscle formation. *Nat. Commun.* *8*, 15664. <https://doi.org/10.1038/ncomms15664>.
- Zhang, W., and Roy, S. (2017). Myomaker is required for the fusion of fast-twitch myocytes in the zebrafish embryo. *Dev. Biol.* *423*, 24–33.

STAR★METHODS

KEY RESOURCES TABLE

REAGENT OR RESOURCE	SOURCE	IDENTIFIER
Antibodies		
Anti-Digoxigenin-AP, Fab fragments	Sigma Aldrich	Cat#:11093274910; RRID: AB_2734716
Rabbit anti GFP pAb antibody	AMSBIO	Cat# TP401; RRID: AB_10890443
beta Catenin antibody [15B8]	Abcam	Cat# ab6301; RRID: AB_305406
Rabbit anti GFP pAb antibody	AMSBIO	Cat# TP401; RRID: AB_10890443
beta Catenin antibody [15B8]	Abcam	Cat# ab6301; RRID: AB_305406
Chemicals, peptides, and recombinant proteins		
Tricaine	Sigma Aldrich	Cat#:A5040
SU-5402	Sigma Aldrich	Cat#:SML0443
Nocodazole	Sigma Aldrich	Cat#:M1404
Critical commercial assays		
DIG RNA Labeling Mix	Roche	Cat#11277073910
SIGMAFAST Fast Red	Sigma Aldrich	Cat#F4648
Experimental models: Organisms/strains		
Zebrafish: <i>Tg(PACprdm1:GFP)</i> ; i106Tg	Roy Lab, Insitute of Molecular and Cell Biology	ZDB-TGCONSTRCT-080923-2
Zebrafish: <i>smo</i> ^{hi1640Tg/hi1640Tg} ; hi1640Tg	Roy Lab, Insitute of Molecular and Cell Biology	ZDB-ALT-011018-4
Zebrafish: <i>prdm1a</i> ^{tp39/tp39} ; tp39	Roy Lab, Insitute of Molecular and Cell Biology	ZDB-ALT-980203-1356
Oligonucleotides		
mymk-forward in situ: ATGCGGATCCCG CAATGGGAGCGTTTATCGCCAAG	This study	N/A
mymk-reverse: ATGCGAGCTCTACACAG CAGCAGAGGGTG TAG	This study	N/A
mymx-forward: ATGCGAATTCCAAAATG CCAGCCGTTTCTCTTGC	This study	N/A
mymx-reverse: ATGCGAGCTCAGTCTT GTTGCTCGCGTGAATT	This study	N/A
Recombinant DNA		
pCS2-Lyn-EGFP	Yin et al., 2018	N/A
pCS2-H2B-mcherry	Yin et al., 2018	N/A
Software and algorithms		
Fiji/Imagej	Schindelin et al., 2012	https://imagej.net/Fiji
MultiStackReg v1.45 plugin	Brad Busse, National Institutes of Health, USA	http://bradbusse.net/MultiStackReg1.45.jar
Turbo reg	Thévenaz et al., 1998	http://bigwww.epfl.ch/thevenaz/turboreg/
Correct 3D drift plugin	Parslow et al., 2014	https://imagej.net/plugins/correct-3d-drift
R Project for Statistical Computing version 4.0.2	R Project for Statistical Computing	http://www.r-project.org/ ; RRID:SCR_001905
Seg ²	This study	https://github.com/tes24/MuscleSeg ; https://doi.org/10.5281/zenodo.7014408
MTrackJ plugin	Meijering et al., 2012	https://imagescience.org/meijering/software/mtrackj/
Rstudio	Rstudio	http://www.rstudio.com/ ; RRID:SCR_000432

RESOURCE AVAILABILITY

Lead contact

Request for resources and data should be directed and will be fulfilled by the lead contact, Timothy E. Saunders (timothy.saunders@warwick.ac.uk)

Materials availability

This study does not generate new materials.

Data and code availability

- All data reported in this paper will be shared by the [lead contact](#) upon request.
- All original code and related data will be shared by the [lead contact](#) upon request.
- Any additional information required to reanalyse the data reported in this paper is available from the [lead contact](#) upon request.

EXPERIMENTAL MODEL AND SUBJECT DETAILS

Zebrafish husbandry

All zebrafish strains were maintained according to standard procedures for fish husbandry at the zebrafish facilities of the Institute of Molecular and Cell Biology and Warwick University. The following wild-type, mutant and transgenic strains were used: AB, inbred wild-type control, *smo*^{hi1640} (Chen et al., 2001), *ubo*^{tp39} (van Eeden et al., 1996) and *Tg(prdm1a::GFP)* (Elworthy et al., 2008). All experiments with the zebrafish in Singapore were approved by the Singapore National Advisory Committee on Laboratory Animal Research. All experiments in Warwick were performed in compliance with the University of Warwick animal welfare and ethical review board (AWERB) and the UK home office animal welfare regulations, covered by the UK Home office licenses PEL 30/2308 and X59628BFC to the University of Warwick.

METHOD DETAILS

Time-lapse imaging

To analyse cell membranes and nuclear dynamics in the myotome, zebrafish embryos were co-injected with 2 nl of *lyn-gfp* and *h2b-mcherry* mRNAs (30 ng/ul each) at the 1-cell stage. Embryos were mounted in low melting agarose (1% diluted in embryo rearing medium) in glass bottom dishes. To ensure normal development of the trunk of the embryo, solidified agar around the trunk was manually dissected allowing unrestricted elongation.

To avoid muscle twitching during imaging, embryos were kept anaesthetised in embryo medium supplemented with tricaine. For long-term imaging a spinning disk confocal microscope was used, equipped with the following components: a Nikon Eclipse Ti inverted microscope, a W1 Yokogawa confocal spinning disk unit, a Photometrics Prime 95B scientific CMOS camera for image detection and a 60x 1.2 NA (numerical aperture) water immersion objective. 488 nm and 561 nm DPSS lasers were used for excitation; laser power was kept at minimum to avoid bleaching of the fluorescent proteins (<5% for 488 nm and <10% for 561 nm). A quad band dichroic for 405/488/561/640 excitation and a 525/30 nm and a 617/73 nm single-band bandpass filters for emission detection and camera exposure was set at 200 milliseconds.

During time lapse, 80-90 focal planes were acquired at z-step of 1 μm and time interval was set at 3 min and imaging was uninterrupted for at least 12 hours. Due to continuous growth of zebrafish trunk, the stage was manually repositioned between timepoints to keep the acquisition of the somite-myotome transition in the field of view. Temperature was kept at 28°C using a stage temperature controller with continuous temperature feedback from a probe submerged in the media. (Julabo, Germany).

Somite alignment

Image preprocessing for somite alignment was done with Fiji (Schindelin et al., 2012). Single files for every timepoint that contain two channels (nuclei and cell membranes) and focal planes were consolidated and saved in one BigTIFF file. Afterwards, tiff files were processed for bleach correction using histogram matching method (bleach correction plugin).

To correct for embryo tail movement during image acquisition we aligned each dataset using a custom Fiji (Schindelin et al., 2012) macro. The macro uses MultiStackReg v1.45 plugin (Thévenaz et al., 1998) from <http://bradbusse.net/downloads.html> (National Institute of Health) (which depends on TurboReg plugin from <http://bigwww.epfl.ch/thevenaz/turboreg/>) to align the images. First, a time series of the most middle z-slice from the membrane channel was extracted from the hyperstack. A rectangular region of interest (ROI) corresponding to a section or the full image was selected on this time series, and ROI was used for finding the rigid body transformation for each frame with respect to the target frame (middle frame). After that, the same transformation matrices were applied for all z planes and for both channels (nuclei and membrane) so that the whole hyperstack was aligned in the same way. For stabilisation of drifting in the Z axis, a customized Correct 3D drift plugin was used (Parslow et al., 2014).

Mutant analysis

ubo and *smo* mutant embryos were selected by observing the phenotype of the anterior somites at 18–20 somite stage. Embryos with U-shaped somites were selected for mounting. After imaging, the identities of the mutant embryos were confirmed by observing the morphological defects as previously reported (Chen et al., 2001; van Eeden et al., 1996).

Drug treatments

Nocodazole (Sigma M1404) was added to embryos at the 20-somite stage for a duration of 4 hours while live imaging. Stocks were prepared in DMSO and diluted to a final concentration of 250 nM in embryo medium. The data in Figure S4E were collected from three embryos (three segments per embryo) for each condition. In total, there were 163 and 146 fusion events in the control and nocodazole treated embryos, respectively. SU5402 experiments were performed as previously described (Yin et al., 2018). We utilised both wild-type (AB) injected with 2 nl of *lyn-gfp* and *h2b-mcherry* mRNAs and *Tg(prdm1a::GFP)* (Video S7) zebrafish embryos.

Cell tracking protocol

Due to rapid cell rearrangements, we found that automated software packages were not capable of segmenting and tracking cells during myotome development. Instead, cell tracking was done manually by localising the middle z plane position of the cell nucleus using Fiji plugin MtrackJ (Meijering et al., 2012). Three researchers, working independently, tracked somites and collated results. The data between all three researchers were consistent, suggesting that the tracking was done with high fidelity. Though slower, this provided highly reliable data. Nuclei positions were exported as csv files and imported in Rstudio running R version 4.0.2. Localisation and tracking of fast and slow muscle population were done as follows: (1) Manual tracking of the fast myocytes was performed by localising the nuclei that corresponded to multinucleated fast muscle in the last timepoint of the imaging (Figures S1B–S1D). (2) The nuclei were back tracked in time and space and the cell fusion time and position was labelled to every fast myocyte trajectory data. (3) The nuclei trajectories that corresponded to a single multinucleated fast muscle were labelled with a unique cell identifier in the dataset. (4) The slow muscles were identified in the last timepoint of imaging by assessing their phenotype. Slow muscles typically are elongated, mononucleated and they are located on the surface of the fast muscle domain, below the enveloping layer (Figure S1B). Due to the characteristic medial to lateral movement of the slow muscles (Figures S1C–S1F), individual slow muscles trajectories were manually checked after tracking to ensure their slow-twitch identity. After tracking was done, fast and slow muscle domains could be easily identified by the total distance moved and average cell speed (Figure S1E), persistence (Figure S1F) and their spatio-temporal movement (Figure S1G). The above procedure is discussed in more detail in Yin et al. (2018).

Cell segmentation

As manual cell segmentation is highly time-consuming, a semi-automated pipeline, which we termed Seg², was developed to assist cell segmentation. In most automated pipelines, incomplete cell segmentations are typically discarded. Due to the image limitations and the highly dynamic nature of the developing myotome, we found that such incomplete cell segmentations were common using available software packages. However, we observed that most failed segmentations were the result of easily identifiable errors, such as split segmentation or membrane gaps. Seg² maintains partial segmentations and then a simple interface enables a user to quickly annotate the preliminary segmentation. This annotated dataset is then fed into a second round of segmentation. We outline the steps below.

Each segmentation round is comprised of the following series of image transformations. First, tracking data were used to subset imaging movies into files containing individual cells (cell file) using a custom macro in Fiji. Then, the cell image was denoised and reconstructed using Richardson-Lucy deconvolution (Lucy, 1974; Richardson, 1972). Next, we used the adaptive thresholding algorithm (implemented using OpenCV) with a means filter (AMT) to separate the cell membrane from the background. Cell seeds were then identified using a hybrid of AMT and distance mapping. AMT was responsible for generating most of the seeds, while distance mapping assisted with picking up smaller seeds that AMT missed. OpenCV's watershedding function was then used to propagate the seeds until membrane boundaries or other propagating segments were reached.

The output of the first segmentation round was inspected by a human who could either leave the segmentation untouched or make annotations to guide the machine in improving the segmentation. These annotations were then fed into another round of segmentation that uses the same steps as the first but modifies the image and segmentation output according to the annotations made.

Fluorescent *in situ* hybridisation

Fluorescent *in situ* hybridization of whole mount zebrafish embryos was performed as previously described (Narayanan and Oates, 2019). The coding regions of *mymk* and *mymx* were cloned from zebrafish cDNA by PCR amplification using the primers:

```
mymk-forward: ATGCGGATCCCGCAATGGGAGCGTTTATCGCCAAG  
mymk-reverse: ATGCGAGCTCTACACAGCAGCAGAGGGTGTAG  
mymx-forward: ATGCGAATTCCAAAATGCCAGCCGTTTCTCTTGC  
mymx-reverse: ATGCGAGCTCAGTCTTGTGTCTCGCGTGAATT.
```

Digoxigenin-labelled RNA probes were transcribed using the DIG RNA Labeling Mix (Roche 11277073910). Zebrafish embryos were fixed at the 22-somite-stage using 4% para-formaldehyde in 1X PBS for 2 hours at room temperature. Embryos were then

dehydrated in methanol, permeabilized using proteinase-K treatment, and hybridized using the DIG-labelled RNA probes at 60°C for 16 hours. Fluorescent staining was performed using an anti-digoxigenin-AP antibody (Roche 11093274910) and SIGMAFAST Fast Red (Sigma F4648). The nuclei were labelled using DAPI (Sigma D9542). For labelling of slow muscle fibres, *Tg(prdm1a::GFP)* expressing embryos were fixed at the 22-somites-stage and stained using an anti-GFP antibody (Amsbio TP401). Cell membranes were labelled using an anti- β -catenin antibody (Abcam ab6301). Embryos were immunostained with primary antibodies at 4°C for 16 hours before proceeding with the fluorescent *in situ* hybridization protocol.

The stained embryos were mounted laterally in 1% agarose after removing the yolk and imaged on a Nikon A1R confocal microscope using a 40x water-immersion objective. The timing of fusion events from live movies was correlated with *mymk* expression in fixed samples by approximating the developmental age of each somite after segmentation. Since a new somite is segmented from the PSM every 30 minutes at 28.5°C (Kimmel et al., 1995), we approximated a 30 minute time difference between each somite, starting with time zero for somite-stage S0.

Data analysis

Nuclei trajectories were analysed using the following R libraries: Data labelling and analysis of nuclei trajectories were done using *tidyverse*; plots were generated with *ggplot2*, data animation for movies were generated with *gganimate*.

QUANTIFICATION AND STATISTICAL ANALYSIS

Figure 2

For Figures 2A–2C, morphology descriptors were measured using Fiji. Binary images of the masks of the cell contours obtained from the Seg² pipeline were measured using the Analyze particle command. Shape index (p) was calculated using the ratio $\text{perimeter}/\text{area}^{1/2}$. To analyse cell morphology asymmetry between pairs of fast myocytes (relative morphospace), morphology descriptors were calculated using larger value of the two cells as the numerator at each time point (hence, the relative value is always greater than 1). 95% confidence interval (CI 95%) was calculated using R (Bunn and Korpela, 2019) defined by $\text{CI 95\%} = \text{mean} + \text{qt}((1-0.95)/2, n - 1) * \text{sem}$ (Figures 2A–2C). For visualising the cell morphology asymmetry between pairs of fast muscle fused cells, image contours of the cells at different time points were overlaid using Temporal-colour code command in Fiji (Figure 2C).

Figure 3

For Figures 3A and 3B, angle of fusion events was binned and plotted as Rose Plots using Matlab. For Figure 3D, fusion location was determined by dividing the cell into three sections: the two tips along the axis of elongation (“tip” defined by 25% of the total length of the cell); and the centre (50% of the total length of the cell). Fusion orientation was defined as end-to-end (cell fusion happening within the “tip” region) and side to side (fusion of two cells aligned parallel along axis of elongation), see Figure 3C. For Figure 3E, we analysed the recoil rate of the membrane after initiation of fusion using Fiji. At each time point we measured the distance between the two ends of the membrane where fusion occurs (as shown in Figure 3C). As the cell size was quite variable, we normalised the distance at each time point by the final separation distance of the two ends as fusion completed.

Figure 4

In Figure 4B, distance between myocyte fusion partners were calculated in R measuring the Euclidean distance between the two fusion cells pairs in AP (x-axis), DV (y-axis) and ML (z-axis). Distance between myocyte fusion partners in the three-dimensions were calculated in R by measuring the Euclidean distance. Standard deviation of the mean is presented as shaded areas in the graphs.

In Figures 4D and 4E, to test whether position of cell nuclei impacts fusion, we used the ‘ERGM’ package (Hunter et al., 2008) in R. We first constructed a perfect matching (that is, a network where each vertex has degree one) between nuclei, where two nuclei were matched if they eventually merged (Figure 4D). We then fitted an Exponential Random Graph Model (ERGM) restricted to perfect matchings, where matchings were also forced to take place only between nuclei within the same somite. We included the sums of absolute distances in the AP, DV and ML axes at time 0 between matched nuclei as model covariates, and we then used the parameter estimates and their standard errors from the fitted model to determine three p-values via a z-test, one for each axis (Figure 4E). We did the same model fitting with the squared distances to check different possible distance parameterisation and achieved similar results. We also confirmed that either analysing somites separately or combining them into one large data set also led to similar conclusions.

Figure 5

Figure 5B: Three embryos were analysed for each condition. Fluorescence intensity of *mymk* FISH was normalised to maximum FISH intensity for each embryo and to average DAPI intensity for each z-stack to adjust for any imaging variations between embryos. Shaded regions represent ± 1 s.d. In Figure 5C, the shaded region was defined by having normalised *mymk* expression above 0.3. In Figure 5E, distance between the slow muscles and the fusion position were calculated by measuring the Euclidean distance in three-dimensions. Briefly, we identified and assigned the closest slow myocyte to the fusion location and measured the distance between the assigned slow muscle and the fusion location along time. Time was reordered so the 95% CI was calculated using R defined by $\text{CI 95\%} = \text{mean} + \text{qt}((1-0.95)-2, n - 1) * \text{sem}$ (Figure 5E).

Figure 6

Figures 6C–6F as described for Figure 5. In Figure 6F, the Pearson correlation coefficient (R) was calculated using R, ggpubr package and ggscatter for graphs. Probability density was calculated using R, ggplot package and geom_density.

Figure 7

Figures 7C–7F as described for previous figures.

Stochastic model of cell fusion

First, we interpreted the expression profiles of *mymk* to define a region of fusion competency, with a bias towards higher *mymk* expression (assuming observed *mymk* expression roughly correlated with Mymk protein levels in the cell). We set a cut-off to exclude low expression levels (5% maximum signal) and the data was smoothed in the ML axis using a 10 μ m window. We took the data for each somite segment and then interpolated to get a finer time series, taking a period of 30 minutes between somite segments. This expression level was normalised and used to define p_m , the probability of fusion at a particular time given the *mymk* levels. When we considered the role of slow fibres, we included a multiplier term $p_{slow} = e^{-(x - x_{slow})^2 / 2\delta^2}$ where $x_{slow} = v_{slow}t + x_{start}$: v_{slow} represented the speed of the slow fibres, x_{start} was where migration began and δ was a (Gaussian) noise term representing variability in slow fibre movement (parameters shown in Table S1). We took $p_{slow} = 1$ once the fibres migrated through the tissue ($x_{slow} > 40\mu m$). We also compared our model prediction when fusion was random throughout the developing myotome (Figures S6G–S6J). Finally, we included a background noise term ϵ , representing noise in the cell positioning. To run the simulation, for each run we generated a uniform random number between $t = 0$ and $t = 240$ min. We then generated the probability distribution for position along the ML axis at that time, $p_{ML}(t)$. Finally, we generated a second random number to determine where, determined by $p_{ML}(t)$, the fusion event occurred along the ML axis. All simulations were run in Matlab. To fit the data, we took a parsimonious approach, where we kept parameters similar across different conditions unless there was a clear reason to change. In *ubo* mutants, we still considered slow fibres to have a role (though they are slower and more dispersed), but there was increased noise (ϵ). In SU5402 treated condition, we modelled the slow fibres as slow and starting later in their movement. *sno* mutants were consistent with *mymk* distribution combined with increased noise.